© 2021. Published by The Company of Biologists Ltd | Journal of Cell Science (2021) 134, jcs254227. doi:10.1242/jcs.254227

RESEARCH ARTICLE

Structural organization of the C1b projection within the ciliary central apparatus

Kai Cai[1,‡], Yanhe Zhao[1,‡], Lei Zhao[2,*,‡], Nhan Phan[1], Yuqing Hou[2], Xi Cheng[2], George B. Witman[2] and Daniela Nicastro[1,§]

ABSTRACT

Motile cilia have a '9+2' structure containing nine doublet microtubules and a central apparatus (CA) composed of two singlet microtubules with associated projections. The CA plays crucial roles in regulating ciliary motility. Defects in CA assembly or function usually result in motility-impaired or paralyzed cilia, which in humans causes disease. Despite their importance, the protein composition and functions of most CA projections remain largely unknown. Here, we combined genetic, proteomic and cryo-electron tomographic approaches to compare the CA of wild-type *Chlamydomonas reinhardtii* with those of three CA mutants. Our results show that two proteins, FAP42 and FAP246, are localized to the L-shaped C1b projection of the CA, where they interact with the candidate CA protein FAP413. FAP42 is a large protein that forms the peripheral 'beam' of the C1b projection, and the FAP246–FAP413 subcomplex serves as the 'bracket' between the beam (FAP42) and the C1b 'pillar' that attaches the projection to the C1 microtubule. The FAP246–FAP413–FAP42 complex is essential for stable assembly of the C1b, C1f and C2b projections, and loss of these proteins leads to ciliary motility defects.

KEY WORDS: Central pair complex, Axoneme, Flagella, Cryo-electron tomography, Subtomogram averaging

INTRODUCTION

Cilia are highly conserved organelles in eukaryotes, where they play a variety of roles in cells, including motility, generating fluid flow and sensing extracellular signals. A wide range of human diseases, known as ciliopathies, are associated with cilia dysfunction, leading to symptoms including chronic respiratory infections, laterality abnormalities and infertility (Afzelius, 2004; Braun and Hildebrandt, 2017; Brown and Witman, 2014). The core component of the motile cilium is the '9+2' axoneme, which consists of nine outer doublet microtubules (DMTs) and a central apparatus (CA) composed of two singlet microtubules and associated projections. Each DMT consists of many copies of 96-nm-long units that repeat along the axoneme; each repeat includes major substructures such as outer and inner dynein arms (ODAs and IDAs, respectively), radial spokes (RSs), and nexin–dynein regulatory complexes (N-DRCs) (Fig. 1A). Together with the CA, these substructures produce and regulate the cilium's motility (Dymek and Smith, 2007; Gui et al., 2019; Kikkawa, 2013; Lin and Nicastro, 2018; Loreng and Smith, 2017; Nicastro et al., 2006; Roberts et al., 2013; Viswanadha et al., 2017).

The CA is the largest ciliary regulatory complex. The two singlet microtubules, termed C1 and C2, are both canonical 13-protofilament microtubules; however, they differ in stability and associated projections. Recent cryo-electron tomography (cryo-ET) studies of the *Chlamydomonas reinhardtii* axoneme have identified at least 11 protein projections with a total molecular mass of greater than 14 MDa that form 16- or 32-nm repeating units along the C1 and C2 microtubules (Carbajal-González et al., 2013). Among the 11 projections, six (C1a–C1f) are associated with the C1 microtubule and five (C2a–C2e) are associated with the C2 microtubule (Fig. 1B; Movie 1). The projections consist of many proteins that connect the C1 and C2 microtubules and/or extend toward the RS heads. Presumably the CA regulates ciliary motility through the CA–RS–N-DRC–IDA signaling pathway (Wirschell et al., 2009); however, the molecular details are still elusive. The CA is essential for normal ciliary motility from *Chlamydomonas* to mammals, and mutations affecting the CA often lead to impaired or paralyzed cilia (Dutcher et al., 1984; Smith and Lefebvre, 1996; Smith and Yang, 2004; Witman et al., 1978). In mice and humans, defects in CA proteins are associated with the ciliopathy primary ciliary dyskinesia (PCD) (Loreng and Smith, 2017; Poprzeczko et al., 2019; Teves et al., 2016). For instance, defects in the C1d proteins FAP221 (also known as PCDP1 or CFAP221) or FAP54 (also known as CFAP54) lead to typical PCD symptoms in mice, including accumulation of mucus in the lungs, male infertility and hydrocephalus (Lee et al., 2008; McKenzie et al., 2015). In humans, mutations in the CA protein PF20 (human SPAG16L) can cause male infertility, and recessive mutations in the C2b protein HYDIN cause PCD (Olbrich et al., 2012; Zhang et al., 2007). Therefore, it is important to establish a detailed understanding of CA structures and the mechanisms by which the CA regulates ciliary motility.

Despite the importance of the CA for ciliary motility, the specific locations of most of its proteins remain unknown, which makes the CA the least understood axonemal structure to date. Several recent proteomic and structural studies have shed light on the protein composition and 3D structure of the CA (Carbajal-González et al., 2013; Dai et al., 2020; Fu et al., 2019; Zhao et al., 2019). For example, proteomic comparisons of CAs from wild-type (WT) and CA-mutant *Chlamydomonas* have identified 37 and 44 new candidate CA proteins, respectively (Dai et al., 2020; Zhao et al., 2019), many of which have been assigned to the C1 or C2 microtubule and some to specific projections (Fig. 1B). Our previous cryo-ET study visualized the CA structure with up to

[1]Departments of Cell Biology and Biophysics, University of Texas Southwestern Medical Center, Dallas, TX 75231, USA. [2]Division of Cell Biology and Imaging, Department of Radiology, University of Massachusetts Medical School, Worcester, MA 01655, USA.
*Present address: Tianjin Institute of Industrial Biotechnology, Chinese Academy of Sciences, Tianjin 300308, China.
‡These authors contributed equally to this work.

§Author for correspondence (daniela.nicastro@utsouthwestern.edu)

K.C., 0000-0002-4771-7450; Y.Z., 0000-0001-5777-0055; N.P., 0000-0003-0155-0699; G.B.W., 0000-0002-9497-9218; D.N., 0000-0002-0122-7173

Handling Editor: Guangshuo Ou
Received 7 October 2020; Accepted 29 September 2021

Journal of Cell Science (2021) 134, jcs254227. doi:10.1242/jcs.254227

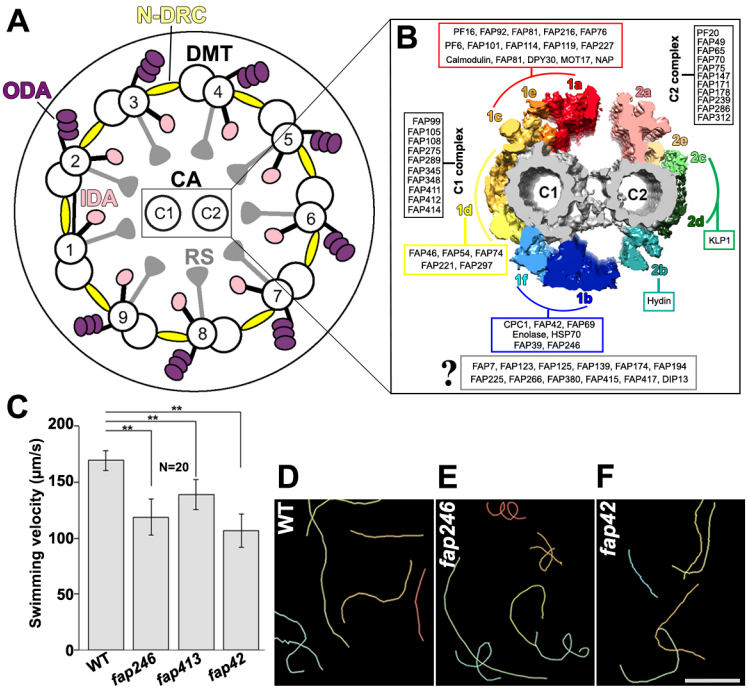

Fig. 1. Known structure and proteome of the CA, and motility phenotypes of *Chlamydomonas* CA mutants. (A) Schematic of a *Chlamydomonas* flagellum in cross-sectional view, showing the DMTs with IDAs and ODAs, N-DRCs, and RSs that project toward the CA. The cross-section is viewed from the proximal end (flagellar base). Box indicates the CA region shown in B. (B) Isosurface rendering of the averaged *Chlamydomonas* CA in cross-sectional view (from the proximal end) and predicted locations of CA proteins based on previous proteomic studies (Zhao et al., 2019). Naming and coloring of CA projections are adapted from Carbajal-Gonzalez et al. (2013) and Fu et al. (2019) using our data. (C) Average swimming velocities of WT *Chlamydomonas* and the three CA mutants *fap246*, *fap413* and *fap42*. Mean±s.d. of n=20 cells. $^{**}P<0.01$ (two-tailed, paired Student's t-test). (D–F) Swimming trajectories of *Chlamydomonas* WT and CA mutants *fap246* and *fap42*. Each colored line represents the swimming path of one cell recorded for 2 s. Scale bar: 100 µm.

2.3 nm resolution and provided details about the molecular architecture of the PF16-dependent C1a–e–c supercomplex, which contains at least 16 proteins (Fu et al., 2019). However, due to the high connectivity within and between CA projections, the assignment of CA proteins to certain projections based on biochemical and mass spectrometry (MS) data can lead to ambiguous or even erroneous conclusions. For instance, the two CA proteins FAP76 and FAP81 were unambiguously shown to be components of the C1a–e–c supercomplex by cryo-ET studies (Fu et al., 2019), but were originally mistakenly assigned to the C1d projection in a preprint version of a proteomic study (Dai et al., 2019 preprint; see Dai et al., 2020 for final results). Given this caveat, it is important to complement MS studies with structural studies by, for example, using cryo-ET of mutants or tagged candidate proteins, to localize specific subunits within the CA.

The C1b projection is one of the largest and most complex CA projections. Pioneering studies on this projection in *Chlamydomonas* have shown that it physically interacts with the C2b projection of the C2 microtubule, and that the *cpc1* mutant, which swims slowly due to reduced ciliary beat frequency, lacks the entire C1b projection, as assessed using conventional electron microscopy (EM), suggesting that the C1b projection has a role in the control of beat frequency (Mitchell and Sale, 1999). Biochemical analyses have found that the *cpc1* axonemes lack three proteins that co-sediment as part of a larger complex, termed the CPC1 complex, which contains at least six proteins (Mitchell and Sale, 1999). Further analysis has identified five of these proteins as CPC1, FAP42, FAP69, enolase and HSP70A (Fig. 1B) (Mitchell et al., 2005). The first cryo-ET study of the CA (Carbajal-González et al., 2013) revealed that the C1b projection is more architecturally complex than previously known, and that its estimated mass is nearly 2 MDa – twice the sum of the masses of the known C1b subunits (883 kDa). Cryo-ET has also shown that C1b interacts with a previously undescribed projection, C1f, which is located between the C1b and C1d projections (Carbajal-González et al., 2013). In our previous analyses of the CA proteome, we identified two novel CA candidate proteins, FAP39 and FAP246, which were assigned to the C1 microtubule and co-immunoprecipitated with known C1b proteins, indicating that they likely are C1b or C1f proteins. We also found that axonemes of the mutant *fap246-1* had greatly reduced amounts of both FAP246 and another candidate CA protein, FAP413, which was predicted to be a C1 protein, but could not be assigned to a specific projection (Zhao et al., 2019). However, none of these proteins have been localized precisely within the CA projections.

Here, we integrated genetic and quantitative proteomic approaches with cryo-ET and subtomogram averaging to compare CAs from WT *Chlamydomonas* and mutants for FAP42, FAP246 and FAP413. The mutants showed impaired motility compared to WT, indicating the importance of the mutated proteins for the regulation of ciliary beating. Our data allowed localization of FAP42, FAP246 and FAP413 within the C1b projection, as well as refined predictions for the locations of FAP39 and six additional CA proteins. 3D classification of the CA structures of the mutants revealed that the FAP246–FAP413–FAP42 subcomplex is critical for the stability of neighboring structures and may play a role in mechanosignaling from the CA to the RS and dyneins to regulate ciliary beating.

RESULTS

Chlamydomonas fap246, *fap42* and *fap413* mutants have motility defects

Chlamydomonas FAP246 (Cre14.g618750.t1.1) is a 120 kDa protein that is predicted to contain conserved leucine-rich repeat (LRR), papain-like and EF-hand domains (Fig. S1A,B). We first re-examined the phenotype of the *fap246-1* (hereafter *fap246*) mutant that was partially characterized in our previous study (Zhao et al., 2019). Nearly all *fap246* cells were motile, but they swam ∼30% slower than WT cells (Fig. 1C), a reduction in swimming velocity slightly greater than we previously reported (possibly reflecting culture in liquid TAP medium here versus culture in modified M medium previously). Compared to WT cells, many *fap246* cells also had an altered swimming pattern in which cells frequently changed swimming direction, resulting in abnormally curved and spiraling swimming paths (Fig. 1D,E). This suggests that FAP246 plays a role in controlling flagellar motility. The reduction of the swimming

Journal of Cell Science (2021) 134, jcs254227. doi:10.1242/jcs.254227

velocity of *fap246* cells was similar to that of the previously described *cpc1* mutant, which lacks the entire C1b projection (Mitchell and Sale, 1999). The previously reported reduction of swimming velocity in the *cpc1* mutant, to about two-thirds that of WT, has been shown to be due to reduced beat frequency (Mitchell and Sale, 1999). To determine whether this is also the case for *fap246*, we directly compared *cpc1* and *fap246* cells and found that their beat frequencies were reduced to 0.56 and 0.72 of that of WT, respectively (Fig. S2D). This reduction is proportional to the reduction in swimming speed of the two mutants and suggests that for both *cpc1* and *fap246* cells the reduced swimming velocity is mainly due to reduced beat frequency. In addition, *cpc1* cells – like *fap246* cells – had abnormally curved swimming paths with transient events of cell body waggle that occurred more frequently than in WT cells (data not shown). These waggles, in which the cell body rocked back and forth in place, likely were caused by momentary asynchrony of the two flagella (Wan et al., 2014). As with flagellar beat frequency, this phenotype was more severe in *cpc1* than in *fap246*.

FAP42 (Cre12.g519950) is an ∼270 kDa protein that is predicted to contain a highly conserved papain-like domain and four guanylate kinase domains (Fig. S1C,D). We obtained a *fap42* mutant (CLiP ID: LMJ.RY0402.205930) from the *Chlamydomonas* Library Project (CLiP; Li et al., 2016) and, using PCR, confirmed disruption of the *FAP42* gene by the insertion of the cassette in a genetically homogenous clone (Fig. S2A). Compared to WT cells, *fap42* cells swam ∼37% slower (Fig. 1C). Cells of *fap42* swam slightly slower than *fap246*-mutant cells, but their swimming paths were less curved (Fig. 1F). The results suggest that FAP42 is also important for the regulation of flagellar motility.

As detailed in the following subsection, our MS analyses suggested that FAP246 and FAP42 are associated with the algae-specific FAP413 (Cre08.g364000.t1.1), which is a 215 kDa protein predicted to have a large WD40-repeat domain at the C terminus (Fig. S1E) (Zhao et al., 2020). We obtained a *fap413* mutant (CLiP ID: LMJ.RY0402.087215) from CLiP (Li et al., 2016) and, using PCR, confirmed disruption of the *FAP413* gene by the insertion of the cassette (Fig. S2B). The swimming velocity of *fap413* mutant cells showed only ∼10% decrease compared to that of WT cells (Fig. 1C), which is the least disrupted motility phenotype of the mutants analyzed here.

Proteomic studies of *fap246*, *fap42* and *fap413* axonemes

We used quantitative MS to compare the axonemal proteome of WT cells with those of the *fap246*, *fap42*, and *fap413* mutants. Label-free quantitation of proteins across samples was performed using SINQ normalized spectral index software (Trudgian et al., 2011) (Table 1; Table S1). The MS results confirmed that the protein level of FAP246 is greatly reduced in the *fap246* axoneme compared to levels in WT cells (*fap246*/WT ratio=0.05) (Table 1). Only a few unique FAP246 N-terminal peptides were identified in the mutant, suggesting that a small amount of C-terminally truncated FAP246 is assembled into *fap246* axonemes (Table S2). The results also confirmed the previous finding that levels of FAP413, a candidate C1 protein, are reduced in *fap246* axonemes (*fap246*/WT ratio=0.01) (Table 1; Table S2) (Zhao et al., 2019). No other known or predicted CA proteins had similarly reduced levels in *fap246* axonemes.

The MS analysis of *fap413* axonemes showed that FAP413 was absent or greatly reduced compared to levels in WT cells (*fap413*/WT ratio=0) (Table 1). No other known or predicted CA protein, including FAP246 and FAP42, had greatly decreased levels in *fap413* axonemes (Table 1; Table S1).

The MS analyses of *fap42* axonemes revealed that the protein level of FAP42 was greatly reduced in the mutant axonemes compared to levels in WT cells (*fap42*/WT ratio=0.04) (Table 1). The few peptides detected in the mutant originated from throughout the FAP42 sequence (Table S3), suggesting that a small amount of FAP42 is assembled into the *fap42* mutant axoneme. The only other protein that had greatly reduced levels in the *fap42* axoneme was FAP413 (*fap42*/WT ratio=0.03) (Table 1; Table S3). The level of FAP246 in *fap42* axonemes was mildly decreased (*fap42*/WT ratio=0.75) (Table 1).

Taken together, the MS results indicate that FAP413 is dependent on both FAP42 and FAP246 for its assembly into the axoneme, but not vice versa. FAP246 is moderately dependent on FAP42 for its stable assembly into the axoneme. The results strongly suggest that FAP413 interacts with FAP42 and FAP246, and that the three proteins are part of the same complex.

Several other proteins have been shown or predicted to be in the C1b projection, including CPC1, FAP39, FAP69, the chaperone HSP70A, the glycolytic enzyme enolase and, with less confidence, FAP174 and FAP380 (Fig. 1B) (Mitchell et al., 2005; Zhang and Mitchell, 2004; Zhao et al., 2019). Our MS analyses showed that the levels of these proteins were not greatly affected in *fap246* or *fap413* axonemes. In *fap42* axonemes, the levels of FAP69 and CPC1 were also not affected, but the levels of HSP70A, enolase, FAP39 and FAP380 were reduced to 40%, 64%, 33% and 40% of the WT level, respectively (Table 1; Table S1). HSP70A and enolase are known to be located not only to the C1b projection but also elsewhere in the

Table 1. Tandem MS analysis of the axonemes of the *fap246*, *fap413* and *fap42* mutants, showing CA proteins predicted to be localized to the C1b projection

Protein[a]	CA projection	Phytozome gene number	Molecular mass (kDa)	Number of unique peptides				Quantification ratio[b]		
				WT	*fap246*	*fap413*	*fap42*	*fap246*/WT	*fap413*/WT	*fap42*/WT
FAP246	C1b	Cre14.g618750	120	**46**	**8**	50	36	**0.05**	0.81	0.75
FAP42	C1b	Cre12.g519950	262	**135**	137	136	**29**	1.02	0.92	**0.04**
FAP413	C1b	Cre08.g364000	215	**44**	**2**	**0**	**10**	**0.01**	**0.00**	**0.03**
CPC1	C1b	Cre03.g183200	200	118	112	120	119	0.98	1.03	1.18
FAP69	C1b	Cre03.g168200	110	45	45	42	45	1.03	0.67	1.03
HSP70A	C1b	Cre08.g372100	71	47	44	46	40	0.79	0.88	0.40
Enolase	C1b	Cre12.g513200	52	36	35	36	35	0.85	1.22	0.64
FAP39	C1b	Cre02.g145100	127	29	27	35	16	0.83	3.31	0.33
FAP174	C1b or C2b	Cre02.g105950	10	6	6	7	5	1.09	0.81	0.71

[a] FAP246, FAP413 and FAP39 are novel proteins that were predicted to be CA proteins in our previously published proteomic study (Zhao et al., 2019).
[b] Unique peptide numbers that are missing or significantly reduced with mutant/WT ratios <0.2 (or number of peptides <0.5 of WT) are highlighted in bold.

Journal of Cell Science (2021) 134, jcs254227. doi:10.1242/jcs.254227

flagellum or axoneme (Mitchell et al., 2005; Zhao et al., 2019). It is not possible from these results alone to know whether the amounts of HSP70A and enolase remaining in *fap42* axonemes represent only the non-C1b pool, or the non-C1b pool plus a fraction of the C1b pool. In either case, the amounts of these proteins lost from the C1b projection of *fap42* axonemes are likely to be greater than the percentage lost from the entire sample as reported by MS. None of the known proteins in the C1a–e–c supercomplex or C1d projection were significantly affected in any of the three mutants (*fap246*, *fap42* and *fap413*) (Table 1; Table S1).

FAP246 and FAP413 form a complex that is localized to the C1b projection

We next carried out cryo-ET and subtomogram averaging to investigate the CA structure of the *fap246* mutant and compare it with that of the WT CA. Our subtomogram averages revealed the CA structures of WT and *fap246* axonemes with 2.3 nm and 2.2 nm resolution, respectively [Fourier shell correlation (FSC) 0.5 criterion] (Fig. S2C), similar to what we reported previously (Fu et al., 2019). In WT axonemes, C1b is one of the largest CA projections (~1.3 MDa). In cross-sectional view, C1b has a roughly triangular shape. We named the three sides of the triangle (1) the 'pillar', which projects 17 nm outwards from C1 protofilament 9; (2) the 'beam', a long component perpendicular to the pillar at the periphery of the projection; and (3) the 'bracket', which connects diagonally between pillar and beam (Fig. 2A–D and inset). Morphologically, the bracket density consists of two subareas: the slightly more distal 'outer bracket' spans the entire diagonal and connects the beam and pillar, whereas the more proximal 'inner bracket' density attaches to the outer bracket and forms a small connection to the neighboring C1b repeat (Fig. 2B,D). The beam structure extends longitudinally and forms a large connection with the beam structures of the neighboring repeats along the axoneme length. The tip of the beam also connects with the tip of the C2b projection (Movie 1). All C1b structures have a 16 nm periodicity and form multiple connections to neighboring CA structures.

In the *fap246*-mutant structure, the averaged CA repeat lacked the entire bracket density of the C1b projection, confirming that FAP246 is a C1b protein (Fig. 2E–H; Fig. S4C,D). The molecular mass of the FAP246-dependent bracket density was estimated to be ~350 kDa based on the volume difference between the mutant and WT CA average (for details see Materials and Methods). This suggested that the bracket either contains three copies of FAP246 (120 kDa) or additional C1b subunit(s). The only protein besides FAP246 with significantly reduced levels in the MS analyses of *fap246* axonemes was FAP413 (215 kDa). Previously, FAP413 has been predicted to be a C1 protein but could not be assigned to a specific projection (Zhao et al., 2019). Our molecular mass estimates for the densities missing in the *fap246* CA are in good agreement with the combined predicted masses of FAP246 and

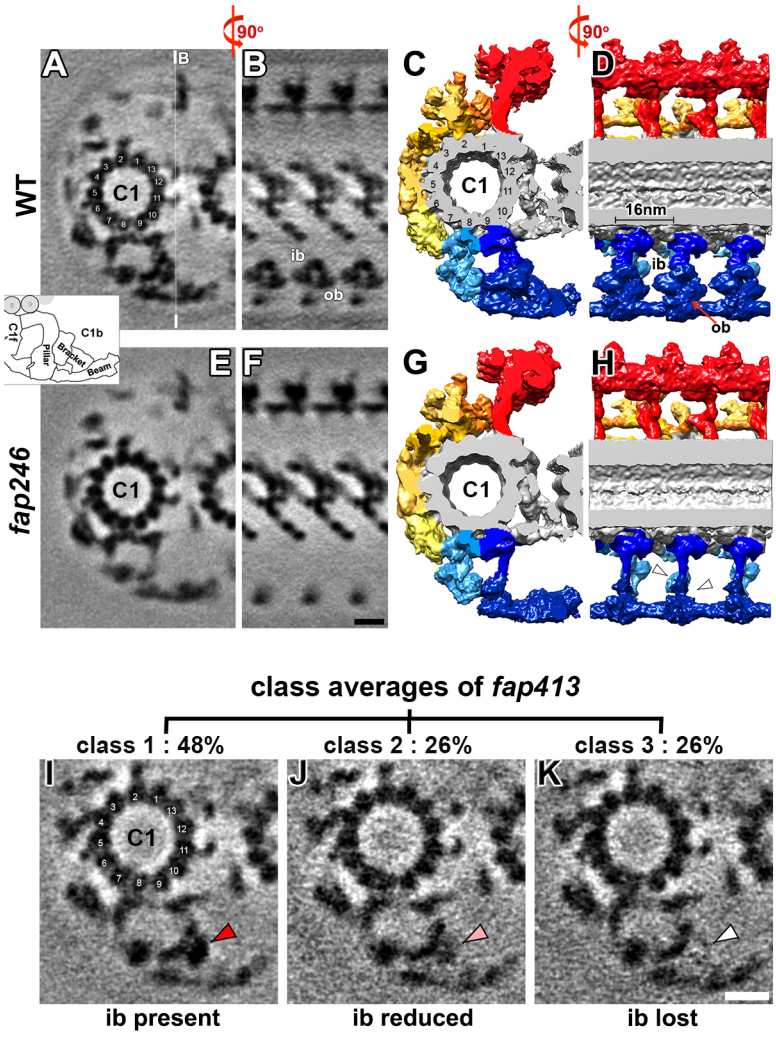

Fig. 2. Cryo-ET and subtomogram averaging of the *fap246* CA reveals defects in the C1b projection, and 3D classification of the *fap413* CA reveals partial loss of the bracket density. (A–H) Tomographic slices (A,B,E and F) and isosurface renderings (C,D,G and H; color-coded as in Fig. 1B) of the averaged CA repeats of WT (A–D) and *fap246* (E–H) in cross-sectional (A,C,E and G; viewed from the proximal end) and longitudinal (B,D,F and H) views show that the C1b inner and outer bracket (ib and ob, respectively) densities are present in WT but missing in *fap246* (white arrowheads). The thin white line in A indicates the position of the slices shown in B and F. In longitudinal slices, the proximal side is on the left. Inset, schematic of the C1b projection shows pillar, bracket and beam regions. Scale bar: 10 nm (shown in F, valid for A,B,E and F). (I–K) 3D classification focused on the bracket region of the *fap413* CA average revealed three distinct classes (percentages of repeats are indicated for each class). Cross-sectional views (viewed from the proximal end) of the class averages show the presence (red arrowhead in I), reduction (pink arrowhead in J) and loss (white arrowhead in K) of the inner bracket density. Scale bar: 10 nm (shown in K, valid for I–K). In A,C,I, numbers indicate the protofilament numbers of C1.

Journal of Cell Science

Journal of Cell Science (2021) 134, jcs254227. doi:10.1242/jcs.254227

FAP413, suggesting that they form the bracket subcomplex, with FAP246 being required for stable assembly of FAP413. The inner bracket is estimated to be slightly larger (~180 kDa) than the outer bracket (~150 kDa) density in the WT structure. However, without knowing the 3D structures of FAP413 and FAP246, we cannot distinguish whether the proteins are globular and arranged next to each other in the inner and outer bracket densities, respectively, or whether their arrangement is more complex, with both proteins being present in the inner and outer bracket structure.

Compared to the WT CA, the density of the pillar and beam appeared to be weakened and blurred in the *fap246* CA average (compare Fig. S3E and F). This blurring suggests either partial reduction of the structures (i.e. not all repeats contain them) or positional flexibility. Therefore, we applied 3D classification focused on the blurred densities (Heumann et al., 2011). Classification of the WT CA structure in this region revealed one structurally homogenous class. In contrast, the C1b structure of *fap246* was separated into four structurally different classes (Fig. S3G–J, Movie 2): in classes 1–3 (Fig. S3G–I) the pillar was present but differently tilted, and in 7% of the repeats the distal half of the pillar was missing (Fig. S3J, class 4). The 3D classification of the blurred beam density also revealed four classes with a comparable distribution as the pillar classes, which is consistent with the pillar and beam forming a unit that moves together. These results showed both positional flexibility and a small reduction of the pillar and beam densities in *fap246*, strongly suggesting that the FAP246–FAP413 bracket plays a role in stabilizing the neighboring C1b pillar and beam. In addition, 3D classification of neighboring CA projections in *fap246* revealed an apparent reduction of the C2b projection in 25% of the repeats (Fig. S3K,L).

We next performed cryo-ET and subtomogram averaging of the *fap413* mutant and visualized its CA with 2.5 nm resolution (FSC 0.5 criterion) (Fig. S2C). Compared to that of the WT structure, the density of the C1b outer bracket was noticeably weakened in *fap413* (compare Fig. S3A,B with Fig. S3C,D). 3D classification focused on the outer bracket density revealed one structurally homogenous class in WT, but three classes in *fap413* (Fig. 2I–K). Specifically, in 48% of the *fap413* CA averages, the inner bracket density was similar to that of WT (class 1, Fig. 2I), in 26% the inner bracket density was weakly visible (class 2, Fig. 2J) and in the remaining 26% the inner bracket density was completely missing (class 3, Fig. 2K). We closely investigated other structures associated with the averaged CA and DMTs, but the only other axonemal structure partially reduced in the *fap413* mutant was the C2b projection, which was lacking or blurred in 47% of the repeats (Fig. S3M,N). Based on the MS results, FAP413 assembly showed a strong dependence on the presence of FAP246, suggesting that FAP413 localizes to the bracket – possibly the inner bracket – of C1b. Possible reasons for why the inner bracket density showed only partial loss in the CA averages of *fap413*, which appears to lack FAP413 based on our MS results, include possible structural rearrangements or stabilization of otherwise flexible domains from neighboring proteins (e.g. FAP246), or functional redundancy of another protein with FAP413, which is a WD40-repeat protein (Fig. S1E). WD40 repeats are one of the most abundant domains in the eukaryotic genome, and the WD40-repeat protein family is very large (Jain and Pandey, 2018). There are many WD40-repeat domain proteins encoded in the *Chlamydomonas* genome and, because of the shared domain organization, some of these have high sequence similarity with FAP413. Redundancy is not unprecedented in the *Chlamydomonas* axoneme; for example, the WD40-rich protein FAP244 has been shown to substitute for another WD40-rich protein, FAP43, resulting in only partial loss of the I1 dynein tether and tether head complex in the corresponding mutants (Fu et al., 2018; Kubo et al., 2018).

FAP42 forms the beam of the C1b projection

FAP42 was one of the five originally identified C1b proteins in the CPC1 complex (Mitchell et al., 2005), but so far it has not been localized within the C1b projection. Using cryo-ET and subtomogram averaging, we visualized the *fap42* CA with 2.5 nm resolution (FSC 0.5 criterion) (Fig. S2C). Compared to the WT CA, the averaged *fap42* CA repeats lacked the entire C1b beam and large parts of the outer bracket density that usually connects to the beam (Fig. 3; Fig. S4E,F). The mass of the entire FAP42-dependent density was estimated to be ~400 kDa: ~300 kDa for the beam and ~100 kDa for the missing part of the outer bracket structure. This suggests that FAP42 (~270 kDa protein) forms the beam structure and that stable assembly of the bracket depends on FAP42.

In the WT CA, the beam is highly connected to the bracket, the peripheral tip of the C1b pillar, the distal tips of neighboring beams and the tip of the C2b projection (Fig. 3A,D,E; Fig. S4A,B;

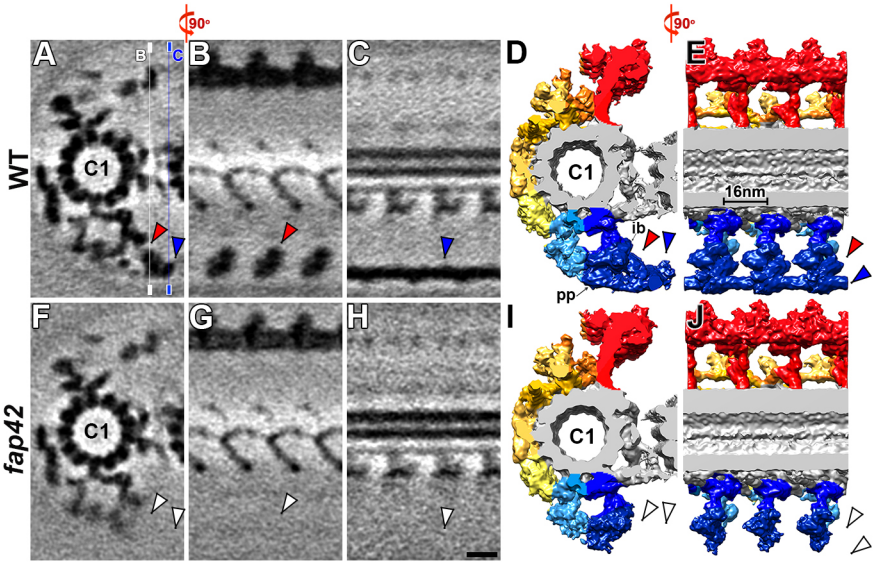

Fig. 3. Cryo-ET and subtomogram averaging localizes FAP42 to the C1b projection. (A–J) Tomographic slices (A–C and F–H) and isosurface renderings (D,E,I and J; color-coded as in Fig. 1B) of the averaged CA repeats of WT (A–E) and *fap42* (F–J) in cross-sectional (A,D,F and I; viewed from the proximal end) and longitudinal views (B,C,E,G,H and J) show that the beam and outer bracket are present in the WT CA repeats (blue and red arrowheads, respectively), but are missing in *fap42* (white arrowheads). The thin lines in A indicate the position of the slices shown in B and G (white line) and in C and H (blue line). In longitudinal slices, the proximal side is on the left. ib, inner bracket; pp, peripheral part of the pillar. Scale bar: 10 nm (shown in H, valid for all EM images).

Journal of Cell Science (2021) 134, jcs254227. doi:10.1242/jcs.254227

Movie 1). Therefore, it is not surprising that several structures in the C1b, C1f and C2b projections that interact with the FAP42-dependent complex were weakened or blurred in the *fap42* structure compared to the WT structure (Fig. 4A–H). We applied automatic 3D classification (Heumann et al., 2011) focusing on these weakened densities, revealing only one structurally homogenous class in the WT structures. In contrast, for *fap42*, two distinct classes were identified for the inner bracket and the peripheral part of the C1b pillar: in class 1 (54%) both bracket densities were present, as in WT (Fig. 4I–K), whereas in class 2 (46%) the entire bracket complex was missing (Fig. 4L–N). For the C1f projection, three classes were identified in *fap42*: in class 1 (50%) the C1f density connecting with the C1b pillar was missing (Fig. 4O,P); in classes 2 and 3 (26 and 24%, respectively) the C1f density was present but showed positional flexibility (Fig. 4Q–T; Movie 3). Similar to *fap246* and *fap413*, the 3D classification of *fap42* revealed that the density of the C2b projection was reduced in 56% of the CA repeats (Fig. S3O,P). In summary, the loss of FAP42 resulted in both reduced occupancy and/or positional flexibility of the C1b bracket and pillar, and of the neighboring C1f and C2b projections. Therefore, FAP42 is essential for the stable assembly and positioning of neighboring structures in the C1b, C1f and C2b projections.

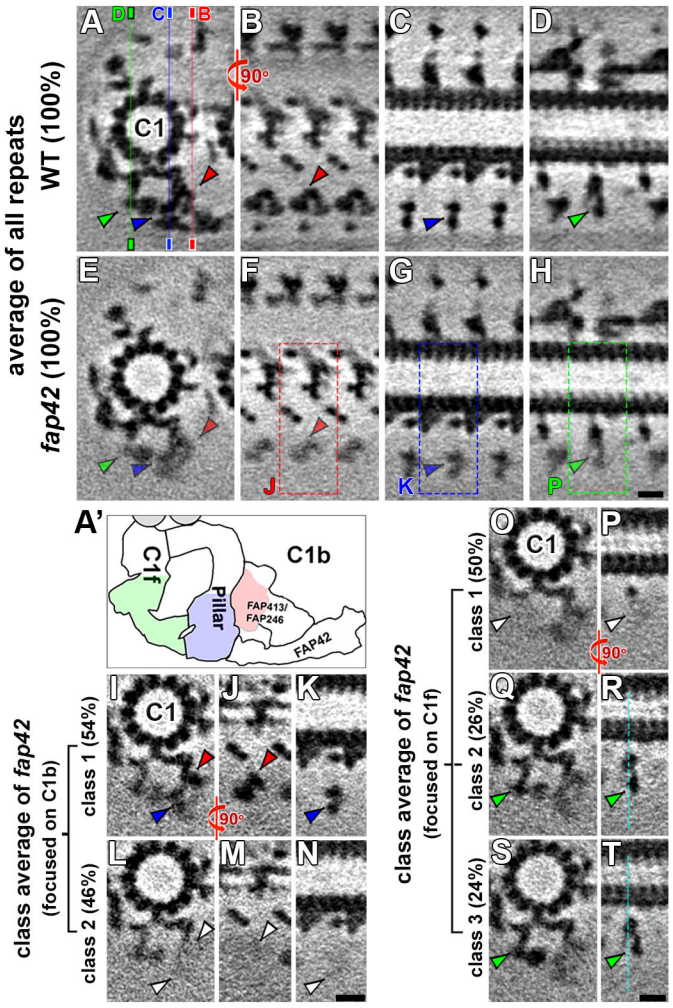

Fig. 4. 3D classification reveals structural heterogeneity for the C1b and C1f projections in *fap42* but not in WT. (A–H) Tomographic slices of averaged CA repeats of WT (A–D) and *fap42* (E–H) axonemes viewed in cross-sectional (A,E; viewed from the proximal end) and longitudinal orientations (B–D and F–H) show that, in addition to lacking the beam and outer bracket density, several C1b and C1f densities, including the inner bracket (red arrowheads), the peripheral part of the pillar (blue arrowheads) and the peripheral part of C1f (green arrowheads) are blurred in the averages of all CA repeats of *fap42* axonemes compared to those of the WT. The thin lines in A indicate the position of the slices shown in B and F (red line), C and G (blue line), and D and H (green line). In longitudinal slices, the proximal side is on the left. Dashed boxes in F,G and H indicate regions shown as separate classes in J,M; K,N; and P,R,T, respectively. (A′) Schematic of the C1b (with pillar, FAP246–FAP413 bracket and FAP42 beam) and C1f projections. The red, blue and green colored regions indicate regions that are blurred in the average of all *fap42* CA repeats, as shown in E–H. (I–T) 3D classification focused on the peripheral regions of C1b (I–N) and on C1f (O–T) reveals distinct classes (percentages of repeats are indicated for each class). Cross-sectional (I,L,O,Q and S; viewed from the proximal end) and longitudinal views (J,K,M,N,P,R and T). In longitudinal slices, the proximal side is on the left. The red, blue and green arrowheads indicate presence of densities, whereas the white arrowheads indicate missing densities. The turquoise dotted lines in R and T serve as references to show the positional differences of structures in different classes. Scale bars: 10 nm (in H, valid for A–H; in N, valid for I–N; in T, valid for O–T).

C1b pillar interacts with several structures in the C1b and C1f projections

Our cryo-ET results showed that the C1b pillar is highly connected with neighboring CA structures through six interfaces (Fig. 2A,C; Fig. 5). Specifically, we observed two connections from the pillar within the C1b projection: to the FAP42 beam (Fig. 5A–C, green) and to the FAP246–FAP413 bracket (Fig. 5A–C, yellow and orange). Additional interfaces of the C1b pillar are the attachment site to protofilament 9 of the C1 microtubule, two connections with the C1f projection (Fig. 5C, cyan) and a connection to part of the CA bridge that links the C1 and C2 microtubules (Fig. 5C, gray).

The protein composition of the pillar is unknown and cannot be precisely dissected using the CA mutants studied here because the pillar structure remained mostly present in all three mutants. However, previous studies have predicted five additional C1b proteins, CPC1 (205 kDa), FAP69 (114 kDa), enolase (51 kDa), HSP70A (71 kDa) and FAP39 (127 kDa) (Mitchell et al., 2005; Zhao et al., 2019), which we did not find in the C1b beam and bracket structures. Therefore, the C1b pillar likely contains most or all of these proteins, which in sum would be ∼570 kDa, slightly larger than the estimated total molecular mass of ∼450 kDa for the pillar based on the cryo-ET averages.

DISCUSSION

Protein composition and structural organization of the C1b projection

The CA is highly conserved and plays essential roles in regulating ciliary beating, likely through the CA–RS–IDA–N-DRC–dynein signaling pathway (Wirschell et al., 2009). Single protein mutations often cause CA defects that result in impaired or paralyzed cilia and are associated with various ciliopathies (Loreng and Smith, 2017; Poprzeczko et al., 2019; Teves et al., 2016). Our previous CA study, which combined structural and biochemical data, revealed a 2 MDa C1a–e–c supercomplex (Fu et al., 2019). In the same study, we identified several key proteins in this supercomplex, including PF16, FAP76, FAP81, FAP92 and FAP216, and precisely localized them using cryo-ET (Fu et al., 2019). Our study also highlighted that structural data are often critical for guiding the interpretation of biochemical data. For example, FAP81 has been found to immunoprecipitate with C1a and C1e proteins, but could not be definitively assigned to either of these projections (Zhao et al., 2019); however, our previous cryo-ET study revealed that FAP81

Journal of Cell Science (2021) 134, jcs254227. doi:10.1242/jcs.254227

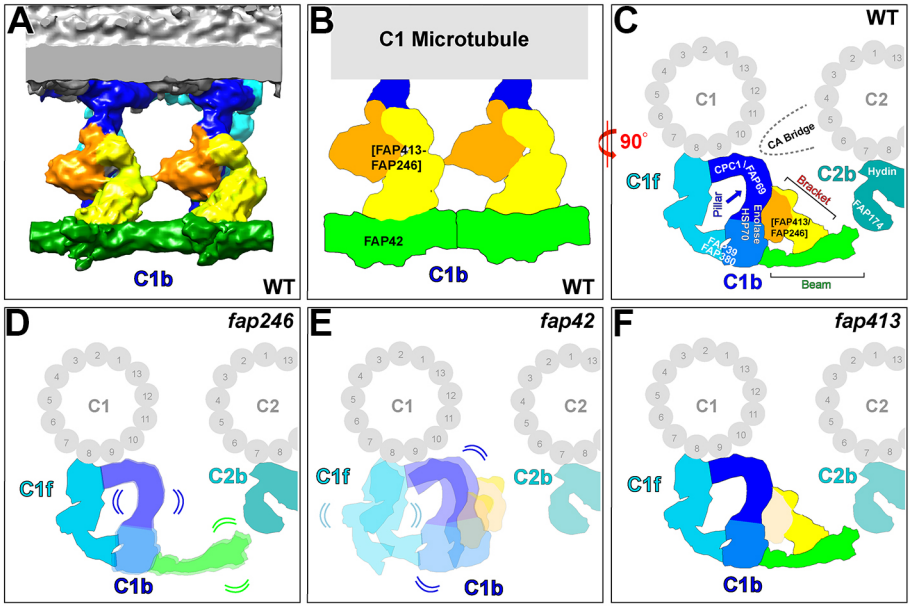

Fig. 5. Summary model depicting the structural organization of the C1b projection and showing the effects of partial loss of the FAP246–FAP413–FAP42 subcomplex on the CA structure. (A–C) The isosurface rendering (A) and schematic drawings (B,C) show part of the 3D structure of the averaged *Chlamydomonas* WT CA repeat viewed in longitudinal orientation (A,B; two 16 nm repeats are shown, with the proximal end to the left) and cross-sectional orientation (C; viewed from the proximal end). The views highlight the subunit organization of the C1b projection, including the FAP246–FAP413 bracket, with the longer 'outer bracket' (yellow) and the attached 'inner bracket' density (orange), and the FAP42 beam (green). In C, the pillar base and peripheral density are shown in dark and medium blue, respectively. The predicted locations of neighboring candidate proteins in the C1b, C1f and C2b projections are indicated in C, along with the C1 and C2 microtubules (numbers indicate protofilament numbers of C1 and C2). Dashed line in C indicates the position of the CA bridge. (D–F) Schematic drawings of the averaged 16 nm CA repeat of *fap246* (D), *fap42* (E) and *fap413* (F) in cross-sectional view (viewed from the proximal end), showing the observed structural CA defects in the mutants compared to the WT CA. In *fap246* the FAP246–FAP413 bracket is missing, and the pillar (base and peripheral density colored dark and medium blue, respectively) and the beam (green) densities show positional flexibility. In *fap42* the beam (FAP42) and partial bracket (FAP413) are missing, and neighboring C1b and C1f densities show positional flexibility and partial reduction. In *fap413* the bracket density (FAP413) is reduced. Compared to the WT structure, the C2b density (turquoise) in all three C1b mutants was reduced, suggesting partial protein loss.

localizes to the C1c projection within the interconnected C1a–e–c supercomplex (Fu et al., 2019). For most of the remaining CA projections, subunits have so far only been characterized biochemically, including for the C1d projection (FAP46, FAP54, FAP74, FAP221 and FAP297) and for the C2b, C2c and C2d projections (Brown et al., 2012; DiPetrillo and Smith, 2010, 2011; Lechtreck and Witman, 2007; Zhao et al., 2019).

The protein composition of the C1b projection has previously been predicted based on co-sedimentation in sucrose gradients, proteomics studies of CA mutants and co-immunoprecipitation assays. The C1b candidate proteins reported previously include CPC1, FAP39, FAP42, FAP69, FAP246, HSP70A, enolase, and – with less confidence – FAP174 and FAP380 (Dai et al., 2020; Mitchell et al., 2005; Zhang and Mitchell, 2004; Zhao et al., 2019). In the present study, we compared axonemes of WT cells and three mutants, *fap42*, *fap246* and *fap413*, using a combination of MS and cryo-ET. We localized FAP42 and FAP246 within the C1b projection, and identified and localized a new C1b subunit, FAP413, which was previously predicted to be a C1 protein (Zhao et al., 2019). Finally, we described the structural organization of the subcomplex formed by these three subunits (Fig. 5; Movie 4).

The C1b projection can be divided into three major structural parts (Fig. 5; Movie 4): (1) FAP42 (Fig. 5, green) forms repeating beams at the interface between the CA and RS heads; (2) the pillar (Fig. 5, blue) attaches the C1b projection to protofilament 9 of the C1 microtubule and is a major interaction hub with five additional interfaces with neighboring CA structures, including C1f and the C1–C2 bridge; and (3) FAP246 and FAP413 (Fig. 5, yellow and orange) form a bracket between the pillar and beam. We named the FAP246–FAP413 complex the 'bracket' because the C1b projection architecture resembles a pillar–beam construction for roofs, and our 3D classification revealed that disruption of the bracket structure in *fap246* and *fap42* mutants resulted in structural destabilization (positional flexibility and reduction) of the remaining C1b and C1f structures. The C1b projection has a 16 nm periodicity along the C1 microtubule, whereas the C1f projection contains structural features that repeat with 32 nm periodicity, similar to the neighboring C1d projection (Movie 1) (Carbajal-González et al., 2013). The bracket structure is not present in the CA of sea urchin sperm flagella (Carbajal-González et al., 2013), consistent with previous phylogenetic analyses showing that FAP413 is limited to green algae and that FAP246 belongs to a sizable group of CA proteins that are members of large protein families or contain common conserved motifs, but may not have true orthologs in metazoans (Zhao et al., 2020). Surprisingly, the beam structure is present in the sea urchin (Carbajal-González et al., 2013), despite FAP42 likely not having a true ortholog in metazoans (Carbajal-González et al., 2013; Zhao et al., 2020). FAP42 is a member of a large protein family (transferases), and it is possible that another family member substitutes for it in metazoans.

A previous study has shown that FAP42 co-sediments with CPC1, FAP69, HSP70A and enolase (Mitchell et al., 2005), and that FAP39 co-immunoprecipitates with HA-tagged FAP246 (Zhao et al., 2019). Abundance of the five previously identified candidate C1b proteins was not greatly reduced in the axonemal proteomes of the three mutants of the C1b beam–bracket (FAP246–FAP413–FAP42) subcomplex studied here (Table 1), suggesting that they might form the C1b pillar, or part of the C1f or C2b projections. Previous

classical EM studies have observed that the entire C1b projection is missing from *Chlamydomonas cpc1* mutant flagella (Mitchell and Sale, 1999; Zhang and Mitchell, 2004). Therefore, CPC1 likely is located at the base of the C1b pillar and serves as a scaffold or docking protein that stabilizes the attachment of C1b to the C1 microtubule, possibly by interacting also on two sides with C1f and/or the C1–C2 bridge (Fig. 5). In contrast to CPC1 and FAP69, which were completely unaffected in our MS of *fap42* and *fap*246 axonemes, the levels of enolase, HSP70A and FAP39 were reduced, with a reduction to 33–64% of the WT levels in *fap42* axonemes (Table 1). Because enolase and HSP70A are known to locate not only to the C1b projection but also elsewhere in the axoneme (Mitchell et al., 2005; Zhao et al., 2019), our MS results likely underestimate the loss of these two proteins from the C1b projection. Especially in *fap42*, enolase and HSP70A could be greatly reduced if not entirely lost from the C1b complex. Overall, this suggests that enolase, HSP70A and FAP39 localize to the peripheral half of the C1b pillar (Fig. 5, medium blue) that connects to FAP42, FAP246 and FAP413, and that was missing in ∼46% of the *fap42* repeats (Fig. 4I–N, class 2) and in 7% of the *fap246* repeats (Fig. S3J, class 4). The estimated size of the pillar region by cryo-ET is ∼450 kDa, which is slightly smaller than the ∼570 kDa sum of the predicted pillar proteins CPC1 (205 kDa), FAP39 (127 kDa), FAP69 (114 kDa), HSP70 (71 kDa) and enolase (51 kDa). However, mass estimations based on cryo-ET averages could be underestimates, because if some of the complex subunits have intrinsically disordered domains or exhibit positional flexibility, these densities would not be well-represented in averages. Alternatively, some of these proteins could belong to the neighboring C1f projection (Fig. 5), which would be consistent with our finding that part of the C1f projection also showed missing density in 50% of the repeats of the *fap42* CA (Fig. 4O,P), similar to the peripheral pillar density.

To date, no C1f proteins have been identified. Our present proteomic analyses of *fap42* axonemes revealed that another candidate CA protein, FAP380 (20 kDa) (Zhao et al., 2019), was reduced to 40% of WT level (Table S1). Given the partial loss of the C1b pillar and C1f projection in the *fap42* mutant, FAP380 may be a subunit of the C1b pillar or C1f projection. None of the known proteins of the C1a–e–c supercomplex or the C1d projection had substantially decreased levels in the C1b mutants studied here (Table 1).

The candidate CA protein FAP174 (10 kDa), which has previously been assigned to C2 (Rao et al., 2016), has also been observed to co-immunoprecipitate with FAP246–HA, and thus is suggested to be a C1b or C2b protein (Zhao et al., 2019). Levels of FAP174 were mildly reduced in our MS analyses of *fap42* and *fap413* axonemes, but were not reduced in *fap246* axonemes. By cryo-ET, the C2b projection was reduced in all C1b mutants studied here, in particular in the *fap42* mutant when the beam structure was missing (Fig. S3P, 56%), suggesting that FAP174 could localize to C2b. Based on our MS results, the proposed C2b protein hydin was still present in the mutant axonemes. Possible explanations could be that hydin – which contains multiple proposed microtubule-binding ASH domains – may detach from C2, but rebind elsewhere on the axoneme (Zhao et al., 2020), or it could become positionally flexible, blurring out in the cryo-ET averages.

C1b proteins contribute to the regulation of ciliary beating

FAP246 contains highly conserved LRR, papain-like and EF-hand domains (Fig. S1A). The mammalian homolog of FAP246, LRGUK (NP_653249) (Fig. S1B), has previously been observed in the mouse spermatid manchette, sperm basal body and flagellum, and seems to be required for sperm assembly (Liu et al., 2015). FAP42 contains four guanylate kinase domains, of which one is highly conserved (Fig. S1C) with similarity to guanylate kinase isoform b (GUK1; NP_000849.1) (Fig. S1D). The latter catalyzes the transfer of a phosphate group from ATP to GMP to form GDP and is a potential cancer chemotherapy target (Khan et al., 2019). Guanylate kinase activity – possibly provided by both FAP42 and FAP246 – has not been studied in cilia, but maintenance of flagellar GTP concentrations may be important for both guanylate cyclase activity and tubulin polymerization (Mitchell et al., 2005). CPC1 contains an adenylate kinase domain, indicating that it might be involved in maintaining stable intraciliary ATP levels during ciliary beating (Zhang and Mitchell, 2004). Another C1b protein, enolase, might also have a role in ATP production in the cilium. In fact, it was previously proposed that reduced flagellar enolase levels in the *cpc1* mutant could cause a reduced ATP concentration in the ciliary matrix, resulting in reduced beat frequency (Mitchell et al., 2005). Although we cannot exclude that reduced enolase activity contributes to the motility defects in C1b mutants, it is likely not the sole factor, because the enolase level was substantially reduced in *fap42*, but only mildly reduced in *fap246*, yet both mutants showed similarly reduced swimming speeds.

All C1b mutants studied so far showed reduced swimming velocity, with the severity ranging from medium in *cpc1*, to mild in *fap246* and *fap42*, and very mild in *fap413*. This is in contrast to mutations of some other CA proteins (such as PF16 and FAP216 from the C1a–e–c supercomplex, and FAP46 and FAP74 from the C1d projection) that cause severely impaired motility or paralyzed cilia (Brown et al., 2012; Dutcher et al., 1984; Fu et al., 2019; Smith and Lefebvre, 1996). This likely means that the C1b projection, including the FAP246–FAP413–FAP42 subcomplex, is not essential for transmission of the signal that regulates dynein activity and thus ciliary beating. However, swimming *cpc1*, *fap246* and, to a lesser extent, *fap42* cells exhibited an abnormally high frequency of cell body waggles. This is typically observed when the two *Chlamydomonas* cilia beat asynchronously, suggesting that the C1b projection has some role in coordinating and/or timing the oscillatory switching of dynein activity to maintain synchrony between the two beating cilia (Polin et al., 2009).

It likely is relevant that hydin knockdown strains, which are observed to lack the C2b projection when assessed by conventional EM, exhibit an unusual form of paralysis that strongly suggests a defect in switching dynein on and off at necessary times in the flagellar beat cycle. Biochemical studies have shown that hydin interacts with the CPC1 complex, and that the attachment of hydin to the C2 microtubule is destabilized in the *cpc1* mutant (Brown et al., 2012; DiPetrillo and Smith, 2011; Lechtreck and Witman, 2007; Mitchell and Sale, 1999; Rupp et al., 2001; Yokoyama et al., 2004; Zhao et al., 2019). These previous findings are consistent with our current cryo-ET results that the C2b density is reduced in the C1b mutants analyzed here. Taken together, the results suggest that the C1b and C2b projections function in concert to regulate the timing of dynein activity.

The FAP246–FAP413–FAP42 subcomplex is part of a large interconnected CA network

A recurring feature of CA projections and subunits is their high connectivity within the projection and with neighboring CA structures, resulting in a massive CA network. For example, we previously showed that the C1a–e–c supercomplex forms multiple internal connections and at least three connections with the neighboring C1d projection (Fu et al., 2019). Here, we found that

Journal of Cell Science (2021) 134, jcs254227. doi:10.1242/jcs.254227

the C1b projection has four internal connections and seven connections with neighboring structures, including with C1f, the C1–C2 bridge and C2b (Fig. 5). Furthermore, 3D classification revealed that loss of any protein of the FAP246–FAP413–FAP42 subcomplex caused positional flexibility and/or partial reduction of the neighboring C1b pillar structure and/or the C1f and C2b projections. The C1f projection is not in direct contact with the FAP246–FAP413–FAP42 subcomplex, and thus is likely affected through its connections with the C1b pillar, suggesting a C1b–f supercomplex. Previous findings have shown that the C1f projection interacts with the C1d projection, because knockdown or mutation of the C1d proteins FAP74 and FAP46, respectively, led to loss of the C1d and C1f projections (Brown et al., 2012). The C1d projection itself interacts with the C1c protein FAP76 from the C1a–e–c supercomplex (Fu et al., 2019). In addition, in our cryo-ET averages of the WT CA, the tip of the C1b beam (FAP42) appears to connect with corresponding structures of the C2b projection, and in all the C1b mutants studied here, the density of C2b was partially reduced. Previous studies have suggested that the C1b and C2b projections physically interact; for example, the C1b and C1f projections (identifiable as the 'sheath' when observed using conventional EM) remain attached to the C2 microtubule when the C1 microtubule is lost from axonemes of the *pf16* mutant, and isolated *cpc1* axonemes lacking the C1b projection also frequently lack the C2b projection (Mitchell and Sale, 1999). Conversely, biochemical studies have shown that the C2b protein hydin remains associated with the C1 microtubule when the C2 microtubule is solubilized by high-salt extraction from WT axonemes (Lechtreck and Witman, 2007). Taking all these data together, a picture of a highly interconnected network emerges that includes at least the C1a,e,c,d,f,b and C2b projections. This also explains why biochemical analyses (such as MS and co-immunoprecipitation) alone may not be sufficient to assign subunits to specific CA projections.

The FAP246–FAP413–FAP42 subcomplex provides mechanical support

In straight flagella, the nine DMTs are cylindrically arranged, and the RSs, which project towards the center of the axoneme, end with their heads on a virtual cylinder with ∼40-nm radius. The two parallel CA microtubules themselves cannot interact with all RS heads at the same time, but the different CA projections, which vary considerably in length, angle and shape, form a dense cylindrical CA network with ∼40-nm radius that interacts with the RSs from all nine DMTs (Nicastro et al., 2005). At the current cryo-ET resolution, there appears to be an ∼5-nm gap between the periphery of the CA projections and the RS heads in straight (inactive) axonemes (Oda et al., 2014). In both forward and backward swimming *Chlamydomonas*, the diameter of the axoneme is greater in the plane of bending of bent regions than in straight regions of the flagellum, presumably due to transverse stress acting across the axoneme during bending (Fig. S5) (Lindemann and Mitchell, 2007). In the bent regions, the two CA microtubules, which in *Chlamydomonas* rotate during flagellar beating, are both in the plane of bending, with the C1 microtubule (predominantly) facing DMT-1, at least in principal bends (Mitchell, 2003). The lateral compression of the axoneme in bent regions implies that the RSs mechanically push against the CA projections in a direction perpendicular to the bending plane. Therefore, the C1a–C2a and C1b–C2b projections would be subject to the greatest compression force by the RSs in the bent region (Fig. S5).

Recent cryo-EM studies have shown that the surfaces of the RS heads facing the CA are negatively charged; therefore, if CA projections are also negatively charged, this could prevent sticking of the projections to the RS heads during CA rotation (Grossman-Haham et al., 2021). FAP42, which comprises the beam and is the part of C1b that would directly interact with the RS heads, is, in fact, a moderately acidic protein (pI=6.1). It will be very interesting to determine the distribution of FAP42 acidic (negatively charged) residues relative to the architecture of the beam.

Unlike, for example, the C1c and C1d projections, which are short and closely associated with the C1 microtubule, the C1b beam, which would be closest to the RS heads, is ∼20 nm away from the C1–C2 bridge without being directly supported by the C1 microtubule. However, the structure of C1b appears to be ideally suited to resist compressive force: the shape of the projection resembles that of an architectural pillar–beam construction that transmits load imposed on a horizontal beam (e.g. by a roof) to a vertical pillar and floor that can resist the compression force. In case of the C1b projection, the compression force imposed by the RSs onto the FAP42 beam could be transmitted through the connection with the pillar and the FAP246–FAP413 bracket onto the pillar and ultimately the C1 microtubule – both of which should provide more resistance to inwardly directed compressive force. In addition, neighboring beams are connected to each other (Fig. 5A,B; Movie 4), which could also distribute force across a sheet-like beam network. Defects in the FAP246–FAP413–FAP42 subcomplex resulted in destabilization of the remaining C1b structures, and of the C1f and C2b projections, even in isolated inactive axonemes (i.e. without compression force imposed by bending), suggesting that the FAP246–FAP413–FAP42 subcomplex does indeed play a role in providing mechanical strength and support. The motility defects seen in *cpc1*, *fap42* and *fap246* mutants may, in part, reflect an abnormal but transient compression-induced partial collapse of the C1f–C1b–C2b network in bent regions of the axoneme during each beat cycle.

Defects in C1b also may affect the regulation of dynein arm activity. Previous studies have shown that mechanical interactions between the CA and RS heads are critical for ciliary motility. For example, Oda and colleagues have shown that in the paralyzed *Chlamydomonas* mutant *pf6*, which lacks most of the C1a–e complex, extending the RS heads by addition of a non-ciliary protein of suitable size (e.g. a BCCP tag) is sufficient to restore flagellar motility (Oda et al., 2014). Oda and colleagues have proposed that the C1a projection interacts mechanically and non-specifically with the RSs of DMTs 2, 3 and 4 to transmit signals to the dynein arms. In the *fap42* and *fap246* mutants, loss of the C1b bracket and beam structures could allow the entire CA to move away from the RSs of DMTs 2, 3, and 4 in bent regions, partially impairing CA–RS mechanosignaling required to activate or inactivate the dynein arms in those regions. The positions of specific projections relative to the DMTs undergoing active sliding in bent regions could explain why loss of different CA projections has different effects on flagellar motility (Brown et al., 2012; DiPetrillo and Smith, 2011; Hou et al., 2021; Lechtreck and Witman, 2007; Mitchell and Sale, 1999; Rupp et al., 2001; Yokoyama et al., 2004; Zhao et al., 2019). Thus, the C1b projection might not only support structural integrity and stability of the CA and axoneme, but the mechanical resistance that it provides might also be necessary for proper mechanosignaling between the CA and RSs to regulate dynein activity and thus ciliary beating.

Journal of Cell Science (2021) 134, jcs254227. doi:10.1242/jcs.254227

MATERIALS AND METHODS

Bioinformatics

Domain predictions of FAP246, FAP42 and FAP413 were performed using PROSITE webserver (http://prosite.expasy.org/) (Sigrist et al., 2013). Sequence alignments and BLAST analyses were performed using the BLAST tool from NCBI (Altschul et al., 1990).

Strains and culture conditions

Chlamydomonas reinhardtii WT strains used were g1 (*nit1*, *agg1*, *mt+*; CC-5415, *Chlamydomonas* Resource Center; https://www.chlamycollection.org) and A54-e18 (CC-2929). A *fap246* mutant was originally obtained from the CLiP collection (CLiP ID: LMJ.RY0402.135524) via the *Chlamydomonas* Resource Center and then crossed to g1; a progeny (135524-8A) was named *fap246-1* and used here, as in our previous study (Zhao et al., 2019). Another CLiP mutant (LMJ.RY0402.2059300) with an insertion in exon 7 of the *fap42* gene (Li et al., 2016) was also obtained from the *Chlamydomonas* Resource Center; analysis by PCR (Fig. S2) revealed that the cells originally supplied were genetically heterogeneous, so they were cloned, and one clone harboring the insertion was named *fap42-1* (referred to here as *fap42*) and used in subsequent experiments. The *fap413* mutant was obtained from the CLiP collection (LMJ.RY0402.087215); loss of *FAP413* was confirmed by PCR analysis (Fig. S2).

As previously described (Fu et al., 2018), *Chlamydomonas* cells were maintained in solid Tris-acetate-phosphate (TAP) plates (supplied with 7.5 µg/ml paromomycin for CLiP mutants) and cultured in liquid TAP medium or modified M medium (Witman, 1986) under a 12:12 h light:dark cycle at 23°C with filtered air bubbling into the growth culture. Insertion sites of CLiP mutant *fap42* were confirmed by PCR using the primers listed in Table S4.

Axoneme preparation

Axonemes of *Chlamydomonas* cells were purified by the pH-shock method as previously described (Song et al., 2015; Witman, 1986). Briefly, cells were cultured in liquid TAP medium, harvested by centrifugation (1100 ***g*** for 5 min) and washed twice with fresh M-N/5 minimal medium (Iomini et al., 2009). The cell pellet was resuspended in pH-shock buffer (10 mM HEPES, 1 mM $SrCl_2$, 4% sucrose and 1 mM DTT, pH 7.4), and 0.5 M acetic acid was added to the buffer to adjust the pH to 4.3. After 80 s, 1 M KOH was added to increase the pH to 7.2. The pH shock treatment was performed on ice. After pH shock, 5 mM $MgSO_4$, 1 mM EGTA, 0.1 mM EDTA and 100 µl protease inhibitor PMSF (Sigma-Aldrich) were added to the solution. The solution was centrifuged (1800 ***g*** for 10 min, 4°C) to separate the detached flagella from the cell bodies. To further purify the flagella, the flagella-containing supernatant was centrifuged twice with a 20% sucrose cushion (2400 ***g*** for 10 min, 4°C). After centrifugation, 1% IGEPAL CA-630 (Sigma-Aldrich) was added to the supernatant for 20 min at 4°C to demembranate the flagella. Axonemes were collected by centrifugation (10,000 ***g*** for 10 min, 4°C), and the freshly isolated axonemes were resuspended in HMEEK buffer (30 mM HEPES, 25 mM KCl, 5 mM $MgSO_4$, 0.1 mM EDTA and 1 mM EGTA, pH 7.2). Axonemal samples were either plunge frozen for cryo-ET or stored at −80°C for biochemical assays or MS.

Analysis of motility phenotypes

All observations and recordings were performed on cells grown in TAP or modified M medium at room temperature. To analyze swimming speed, 100 µl of *Chlamydomonas* cell culture in TAP medium was transferred to a plastic chamber (0.127-mm-deep Fisherbrand UriSystem DeciSlide; Thermo Fisher Scientific). Cells were imaged using a Nikon ECLIPSE LV-N microscope equipped with an Andor Zyla sCMOS Camera. The objective lens used was a Nikon CFI S Plan Fluor ELWD 20× NA 0.45 with a working distance of 8.2–6.9 mm. Movies were recorded at 100 frames/s using NIS-Elements AR (Nikon) software. Swimming speeds were determined using the measurement tools in NIS-Elements AR software. The TrackMate plugin (Tinevez et al., 2017) in Fiji ImageJ was used to trace the swimming trajectory of the cells.

For the flagella beat frequency analyses, cells were grown in 120 ml of modified M medium aerated with 5% CO_2 under a 14:10 h light:dark cycle at 23°C. 180–200 µl aliquots of mid-log phase cells were transferred to an ∼0.6-mm-deep chamber made from two 18×18 mm glass coverslips. Movies were recorded at 478 frames/s using a Nikon DIAPHOT 200 inverted microscope with a Nikon Fluor 10× Ph2 DL objective (NA 0.5) and a ZWO AS1174MM-Cool camera with SharpCap software (Version 3.1.5220.0). Beat frequency was calculated by counting the number of 'back and forth' cell body movements (Kamiya, 2000) in 400 frames when the movies were played at 15–20 frames/s, and then dividing that number by the duration of the movie segment analyzed. At least 50 cells were analyzed for each strain.

Liquid chromatography–mass spectrometry

Axonemal proteins (40 µg) of the WT, *fap42* and *fap246* strains were separated on a 4–12% gradient SDS–polyacrylamide gel (Genscript Biotech). After the dye front migrated on the gel for 3.0–3.5 cm, the gel was stained with Coomassie Brilliant Blue for 30 min and destained until the background was clear. Each gel lane was cut into four slices, and each slice was further excised into pieces of 1 mm^3. In-gel trypsin digestion, liquid chromatography–mass spectrometry (LC-MS) and peptide identification were conducted by the proteomics core facility at the University of Texas Southwestern Medical Center. Briefly, protein gel pieces were digested overnight using trypsin (Pierce) following reduction and alkylation with DTT and iodoacetamide (Sigma-Aldrich). The samples then underwent solid-phase extraction cleanup with an Oasis HLB µElution plate (Waters), and the resulting samples were analyzed by LC-MS, using an Orbitrap Fusion Lumos mass spectrometer (Thermo Electron) coupled to an Ultimate 3000 RSLC-Nano liquid chromatography system (Dionex). Samples were injected onto a 75 µm internal diameter, 75 cm long EasySpray column (Thermo Electron) and were eluted with a gradient from 0–28% buffer B over 90 min. Buffer A contained 2% (v/v) acetonitrile and 0.1% formic acid in water, and buffer B contained 80% (v/v) acetonitrile, 10% (v/v) trifluoroethanol and 0.1% formic acid in water. The mass spectrometer operated in positive ion mode with a source voltage of 1.8 kV and an ion transfer tube temperature of 275°C. MS scans were acquired at 120,000 resolution in the Orbitrap and up to 10 MS spectra were obtained in the ion trap for each full spectrum acquired using higher-energy collisional dissociation (HCD) for ions with charges 2–7. Dynamic exclusion was set for 25 s after an ion was selected for fragmentation. Raw MS data files were converted to a peak list format and analyzed using the central proteomics facilities pipeline (CPFP), version 2.0.3 (Trudgian and Mirzaei, 2012; Trudgian et al., 2010). Peptide identification was performed using the X!Tandem (Craig and Beavis, 2004) and Open MS Search Algorithm (OMSSA) (Geer et al., 2004) search engines against the *Chlamydomonas reinhardtii* protein database, with common contaminants and reversed decoy sequences appended (Elias and Gygi, 2007). Another round of peptide identification search was conducted using a more updated *Chlamydomonas reinhardtii* protein database generated from Phytozome (https://phytozome.jgi.doe.gov/pz/portal.html). Fragment and precursor tolerances of 10 ppm and 0.5 Da were specified, and three missed cleavages were allowed. Carbamidomethylation of Cys was set as a fixed modification and oxidation of Met was set as a variable modification. Label-free quantitation of proteins across samples was performed using SINQ normalized spectral index software (Trudgian et al., 2011).

Cryo-ET

Freshly prepared axonemal samples (30 µl) were gently mixed with 10 µl of 10-fold-concentrated, BSA-coated 10-nm gold solution (Sigma-Aldrich). A 4 µl volume of the solution was applied to a glow-discharged (30 s at 35 mA) copper R2/2 holey carbon grid (Quantifoil Micro Tools). After removing excess liquid by blotting the grid from the back side with Whatman filter paper for 2 s, the grid was plunge frozen into liquid ethane using a homemade plunge freezer. Grids were then stored in liquid nitrogen until use.

Grids were loaded into a Titan Krios transmission electron microscope (Thermo Fisher Scientific) operated at 300 kV. The microscope control

software SerialEM (Mastronarde, 2005) was used to acquire tilt series images in low-dose mode from −60° to 60° with 2° increments using a dose-symmetric tilting scheme (Hagen et al., 2017). For WT axonemes, the images were recorded with a 4000×4000 K2 DDD camera (Gatan) in counting mode (15 frames, 0.4 s exposure time per frame, dose rate of 8 electrons/pixel/s for each tilt image). For *fap246*, *fap42* and *fap413* axonemes, the images were recorded with a 5760×4092 K3 DDD camera (Gatan) in counting mode (10 frames, 0.05 s exposure time per frame, dose rate of 26 electrons/pixel/s for each tilt image). For all strains, the post-column energy filter (Gatan) was operated in zero-loss mode (20 eV slit width), and a VPP (Danev et al., 2014) was used with −0.5 µm defocus. The magnification was set to 26,000, with an effective pixel size of 3.2 Å (K3 camera) or 5.5 Å (K2 camera). The total electron dose per tilt series was limited to ∼100 e/Å^2.

Image processing

In brief, motion correction of the frames was performed using MotionCorr2 (Zheng et al., 2017). IMOD software (Kremer et al., 1996) was used to align the tilt serial images using the 10 nm gold particles as fiducial markers and to reconstruct the tomograms by the weighted back-projection (WBP) approach. For subtomogram averaging, either CA or DMT repeats were picked from the raw tomograms, and alignment and missing-wedge compensated averaging were performed using PEET software (Nicastro et al., 2006), which is integrated in the IMOD software package. The axoneme and CA orientation (proximal to distal) was determined for each tomogram based on both DMT orientation in the axoneme cross-section and initial averages that included only the CA repeats within each tomogram. After the CA polarity and the same center of the repeat were determined for each tomogram, a second alignment was performed combining the CA repeats from all tomograms in the correct orientation and periodicity register. After global alignment of all CA repeats, the alignment of each individual CA microtubule was refined by local alignment of each microtubule and its associated projections separately, while the other microtubule was masked as described previously (Carbajal-González et al., 2013; Fu et al., 2019). Visualization of the 3D structures of the averaged CA repeats was done with the UCSF Chimera package software (Pettersen et al., 2004). For generating isosurface renderings, the same isosurface threshold was applied to the WT and mutant averages. Mass estimations of the protein complexes and subvolumes were calculated using the average density of 1.43 g/cm^3 for proteins (Quillin and Matthews, 2000) and after normalizing the isosurface-rendering threshold to the mass of microtubules in Chimera. Classification analyses used a principal component analysis (PCA) clustering method incorporated in the PEET software (Heumann et al., 2011). The number of tomograms and CA repeats, as well as the estimated resolution of the averages (using FSC 0.5 criterion), are summarized for each strain in Table S5.

Acknowledgements

We thank Dr Andrew Lemoff and the proteomics core facility at the University of Texas Southwestern Medical Center (UTSW) for the liquid chromatography-MS analyses. We thank Dr Christina Baer and the Sanderson Center for Optical Experimentation at the University of Massachusetts Medical School for help with the flagellar beat frequency analysis. We are grateful to Dr Daniel Stoddard for management of the UTSW cryo-electron microscope facility, which is funded in part by a Cancer Prevention and Research Institute of Texas Core Facility Award (RP170644). This research was supported in part by the computational resources provided by the BioHPC supercomputing facility located in the Lyda Hill Department of Bioinformatics, UT Southwestern Medical Center.

Competing interests

The authors declare no competing or financial interests.

Author contributions

Conceptualization: D.N.; Methodology: K.C., Y.Z., L.Z., N.P., D.N.; Validation: K.C., G.B.W., D.N.; Formal analysis: K.C., Y.Z., L.Z., Y.H., X.C., G.B.W., D.N.; Investigation: K.C., Y.Z., L.Z., N.P., Y.H., X.C.; Data curation: K.C.; Writing - original draft: K.C.; Writing - review & editing: K.C., G.B.W., D.N.; Visualization: K.C., Y.Z.; Supervision: D.N.; Funding acquisition: G.W., D.N.

Funding

This study was supported by National Institutes of Health grants R01 GM083122 to D.N. and R35 GM122574 to G.B.W., by a Cancer Prevention and Research Institute of Texas grant RR140082 to D.N., and by the R.W.B. Endowment at the University of Massachusetts Medical School to G.B.W. Deposited in PMC for release after 12 months.

Data availability

The averaged 3D structures of the CA focused on the C1b projection from different strains have been deposited in the Electron Microscopy Data Bank under accession codes EMD-22648 (WT), EMD-22649 (*fap246*), EMD-22651 (*fap42*) and EMD-24489 (class average 3 of *fap413*).

Peer review history

The peer review history is available online at https://journals.biologists.com/jcs/article-lookup/doi/10.1242/jcs.254227.

References

Afzelius, B. A. (2004). Cilia-related diseases. *J. Pathol.* **204**, 470-477. doi:10.1002/path.1652

Altschul, S. F., Gish, W., Miller, W., Myers, E. W. and Lipman, D. J. (1990). Basic local alignment search tool. *J. Mol. Biol.* **215**, 403-410. doi:10.1016/S0022-2836(05)80360-2

Braun, D. A. and Hildebrandt, F. (2017). Ciliopathies. *Cold Spring Harb. Perspect. Biol.* **9**, a028191. doi:10.1101/cshperspect.a028191

Brown, J. M. and Witman, G. B. (2014). Cilia and Diseases. *Bioscience* **64**, 1126-1137. doi:10.1093/biosci/biu174

Brown, J. M., Dipetrillo, C. G., Smith, E. F. and Witman, G. B. (2012). A FAP46 mutant provides new insights into the function and assembly of the C1d complex of the ciliary central apparatus. *J. Cell Sci.* **125**, 3904-3913. doi:10.1242/jcs.107151

Carbajal-González, B. I., Heuser, T., Fu, X., Lin, J., Smith, B. W., Mitchell, D. R. and Nicastro, D. (2013). Conserved structural motifs in the central pair complex of eukaryotic flagella. *Cytoskeleton (Hoboken)* **70**, 101-120. doi:10.1002/cm.21094

Craig, R. and Beavis, R. C. (2004). TANDEM: matching proteins with tandem mass spectra. *Bioinformatics* **20**, 1466-1467. doi:10.1093/bioinformatics/bth092

Dai, D., Ichikawa, M., Peri, K., Rebinsky, R. and Bui, K. (2019). Identification and mapping of central pair proteins by proteomic analysis (version 1). *bioRxiv*, 739383. doi:10.1101/739383

Dai, D., Ichikawa, M., Peri, K., Rebinsky, R. and Bui, K. (2020). Identification and mapping of central pair proteins by proteomic analysis. *Biophys. Physicobiol.* **17**, 71-85. doi:10.2142/biophysico.BSJ-2019048

Danev, R., Buijsse, B., Khoshouei, M., Plitzko, J. M. and Baumeister, W. (2014). Volta potential phase plate for in-focus phase contrast transmission electron microscopy. *Proc. Natl. Acad. Sci. USA* **111**, 15635-15640. doi:10.1073/pnas.1418377111

DiPetrillo, C. G. and Smith, E. F. (2010). Pcdp1 is a central apparatus protein that binds Ca(2+)-calmodulin and regulates ciliary motility. *J. Cell Biol.* **189**, 601-612. doi:10.1083/jcb.200912009

DiPetrillo, C. G. and Smith, E. F. (2011). The Pcdp1 complex coordinates the activity of dynein isoforms to produce wild-type ciliary motility. *Mol. Biol. Cell* **22**, 4527-4538. doi:10.1091/mbc.e11-08-0739

Dutcher, S. K., Huang, B. and Luck, D. J. (1984). Genetic dissection of the central pair microtubules of the flagella of Chlamydomonas reinhardtii. *J. Cell Biol.* **98**, 229-236. doi:10.1083/jcb.98.1.229

Dymek, E. E. and Smith, E. F. (2007). A conserved CaM- and radial spoke associated complex mediates regulation of flagellar dynein activity. *J. Cell Biol.* **179**, 515-526. doi:10.1083/jcb.200703107

Elias, J. E. and Gygi, S. P. (2007). Target-decoy search strategy for increased confidence in large-scale protein identifications by mass spectrometry. *Nat. Methods* **4**, 207-214. doi:10.1038/nmeth1019

Fu, G., Wang, Q., Phan, N., Urbanska, P., Joachimiak, E., Lin, J., Wloga, D. and Nicastro, D. (2018). The I1 dynein-associated tether and tether head complex is a conserved regulator of ciliary motility. *Mol. Biol. Cell* **29**, 1048-1059. doi:10.1091/mbc.E18-02-0142

Fu, G., Zhao, L., Dymek, E., Hou, Y., Song, K., Phan, N., Shang, Z., Smith, E. F., Witman, G. B. and Nicastro, D. (2019). Structural organization of the C1a-e-c supercomplex within the ciliary central apparatus. *J. Cell Biol.* **218**, 4236-4251. doi:10.1083/jcb.201906006

Geer, L. Y., Markey, S. P., Kowalak, J. A., Wagner, L., Xu, M., Maynard, D. M., Yang, X., Shi, W. and Bryant, S. H. (2004). Open mass spectrometry search algorithm. *J. Proteome Res.* **3**, 958-964. doi:10.1021/pr0499491

Grossman-Haham, I., Coudray, N., Yu, Z., Wang, F., Zhang, N., Bhabha, G. and Vale, R. D. (2021). Structure of the radial spoke head and insights into its role in mechanoregulation of ciliary beating. *Nat. Struct. Mol. Biol.* **28**, 20-28. doi:10.1038/s41594-020-00519-9

Gui, L., Song, K., Tritschler, D., Bower, R., Si, Y., Dai, A., Augspurger, K., Sakizadeh, J., Grzemska, M., Ni, T. et al. (2019). Scaffold subunits support associated subunit assembly in the Chlamydomonas ciliary nexin-dynein regulatory complex. *Proc. Natl. Acad. Sci. USA* **116**, 23152-23162. doi:10.1073/pnas.1910960116

Hagen, W. J. H., Wan, W. and Briggs, J. A. G. (2017). Implementation of a cryo-electron tomography tilt-scheme optimized for high resolution subtomogram averaging. *J. Struct. Biol.* **197**, 191-198. doi:10.1016/j.jsb.2016.06.007

Heumann, J. M., Hoenger, A. and Mastronarde, D. N. (2011). Clustering and variance maps for cryo-electron tomography using wedge-masked differences. *J. Struct. Biol.* **175**, 288-299. doi:10.1016/j.jsb.2011.05.011

Hou, Y., Zhao, L., Kubo, T., Cheng, X., McNeill, N., Oda, T. and Witman, G. B. (2021). Chlamydomonas FAP70 is a component of the previously uncharacterized ciliary central apparatus projection C2a. *J. Cell Sci.* **134**, jcs258540. doi:10.1242/jcs.258540

Iomini, C., Till, J. E. and Dutcher, S. K. (2009). Genetic and phenotypic analysis of flagellar assembly mutants in Chlamydomonas reinhardtii. *Methods Cell Biol.* **93**, 121-143. doi:10.1016/S0091-679X(08)93007-7

Jain, B. P. and Pandey, S. (2018). WD40 repeat proteins: signalling scaffold with diverse functions. *Protein J.* **37**, 391-406. doi:10.1007/s10930-018-9785-7

Kamiya, R. (2000). Analysis of cell vibration for assessing axonemal motility in Chlamydomonas. *Methods* **22**, 383-387. doi:10.1006/meth.2000.1090

Khan, N., Shah, P. P., Ban, D., Trigo-Mouriño, P., Carneiro, M. G., DeLeeuw, L., Dean, W. L., Trent, J. O., Beverly, L. J., Konrad, M. et al. (2019). Solution structure and functional investigation of human guanylate kinase reveals allosteric networking and a crucial role for the enzyme in cancer. *J. Biol. Chem.* **294**, 11920-11933. doi:10.1074/jbc.RA119.009251

Kikkawa, M. (2013). Big steps toward understanding dynein. *J. Cell Biol.* **202**, 15-23. doi:10.1083/jcb.201304099

Kremer, J. R., Mastronarde, D. N. and McIntosh, J. R. (1996). Computer visualization of three-dimensional image data using IMOD. *J. Struct. Biol.* **116**, 71-76. doi:10.1006/jsbi.1996.0013

Kubo, T., Hou, Y., Cochran, D. A., Witman, G. B. and Oda, T. (2018). A microtubule-dynein tethering complex regulates the axonemal inner dynein f (I1). *Mol. Biol. Cell* **29**, 1060-1074. doi:10.1091/mbc.E17-11-0689

Lechtreck, K.-F. and Witman, G. B. (2007). Chlamydomonas reinhardtii hydin is a central pair protein required for flagellar motility. *J. Cell Biol.* **176**, 473-482. doi:10.1083/jcb.200611115

Lee, L., Campagna, D. R., Pinkus, J. L., Mulhern, H., Wyatt, T. A., Sisson, J. H., Pavlik, J. A., Pinkus, G. S. and Fleming, M. D. (2008). Primary ciliary dyskinesia in mice lacking the novel ciliary protein Pcdp1. *Mol. Cell. Biol.* **28**, 949-957. doi:10.1128/MCB.00354-07

Li, X., Zhang, R., Patena, W., Gang, S. S., Blum, S. R., Ivanova, N., Yue, R., Robertson, J. M., Lefebvre, P. A., Fitz-Gibbon, S. T. et al. (2016). An indexed, mapped mutant library enables reverse genetics studies of biological processes in Chlamydomonas reinhardtii. *Plant Cell* **28**, 367-387. doi:10.1105/tpc.15.00465

Lin, J. and Nicastro, D. (2018). Asymmetric distribution and spatial switching of dynein activity generates ciliary motility. *Science* **360**, eaar1968. doi:10.1126/science.aar1968

Lindemann, C. B. and Mitchell, D. R. (2007). Evidence for axonemal distortion during the flagellar beat of Chlamydomonas. *Cell Motil. Cytoskeleton* **64**, 580-589. doi:10.1002/cm.20205

Liu, Y., DeBoer, K., de Kretser, D. M., O'Donnell, L., O'Connor, A. E., Merriner, D. J., Okuda, H., Whittle, B., Jans, D. A., Efthymiadis, A. et al. (2015). LRGUK-1 is required for basal body and manchette function during spermatogenesis and male fertility. *PLoS Genet.* **11**, e1005090. doi:10.1371/journal.pgen.1005090

Loreng, T. D. and Smith, E. F. (2017). The central apparatus of cilia and eukaryotic flagella. *Cold Spring Harb. Perspect. Biol.* **9**, a028118. doi:10.1101/cshperspect.a028118

Mastronarde, D. N. (2005). Automated electron microscope tomography using robust prediction of specimen movements. *J. Struct. Biol.* **152**, 36-51. doi:10.1016/j.jsb.2005.07.007

McKenzie, C. W., Craige, B., Kroeger, T. V., Finn, R., Wyatt, T. A., Sisson, J. H., Pavlik, J. A., Strittmatter, L., Hendricks, G. M., Witman, G. B. et al. (2015). CFAP54 is required for proper ciliary motility and assembly of the central pair apparatus in mice. *Mol. Biol. Cell* **26**, 3140-3149. doi:10.1091/mbc.e15-02-0121

Mitchell, D. R. (2003). Reconstruction of the projection periodicity and surface architecture of the flagellar central pair complex. *Cell Motil. Cytoskeleton* **55**, 188-199. doi:10.1002/cm.10121

Mitchell, D. R. and Sale, W. S. (1999). Characterization of a Chlamydomonas insertional mutant that disrupts flagellar central pair microtubule-associated structures. *J. Cell Biol.* **144**, 293-304. doi:10.1083/jcb.144.2.293

Mitchell, B. F., Pedersen, L. B., Feely, M., Rosenbaum, J. L. and Mitchell, D. R. (2005). ATP production in Chlamydomonas reinhardtii flagella by glycolytic enzymes. *Mol. Biol. Cell* **16**, 4509-4518. doi:10.1091/mbc.e05-04-0347

Nicastro, D., McIntosh, J. R. and Baumeister, W. (2005). 3D structure of eukaryotic flagella in a quiescent state revealed by cryo-electron tomography. *Proc. Natl. Acad. Sci. USA* **102**, 15889-15894. doi:10.1073/pnas.0508274102

Nicastro, D., Schwartz, C., Pierson, J., Gaudette, R., Porter, M. E. and McIntosh, J. R. (2006). The molecular architecture of axonemes revealed by cryoelectron tomography. *Science* **313**, 944-948. doi:10.1126/science.1128618

Oda, T., Yanagisawa, H., Yagi, T. and Kikkawa, M. (2014). Mechanosignaling between central apparatus and radial spokes controls axonemal dynein activity. *J. Cell Biol.* **204**, 807-819. doi:10.1083/jcb.201312014

Olbrich, H., Schmidts, M., Werner, C., Onoufriadis, A., Loges, N. T., Raidt, J., Banki, N. F., Shoemark, A., Burgoyne, T., Al Turki, S. et al. (2012). Recessive HYDIN mutations cause primary ciliary dyskinesia without randomization of left-right body asymmetry. *Am. J. Hum. Genet.* **91**, 672-684. doi:10.1016/j.ajhg.2012.08.016

Pettersen, E. F., Goddard, T. D., Huang, C. C., Couch, G. S., Greenblatt, D. M., Meng, E. C. and Ferrin, T. E. (2004). UCSF Chimera–a visualization system for exploratory research and analysis. *J. Comput. Chem.* **25**, 1605-1612. doi:10.1002/jcc.20084

Polin, M., Tuval, I., Drescher, K., Gollub, J. P. and Goldstein, R. E. (2009). Chlamydomonas swims with two "gears" in a eukaryotic version of run-and-tumble locomotion. *Science* **325**, 487-490. doi:10.1126/science.1172667

Poprzeczko, M., Bicka, M., Farahat, H., Bazan, R., Osinka, A., Fabczak, H., Joachimiak, E. and Wloga, D. (2019). Rare human diseases: model organisms in deciphering the molecular basis of primary ciliary dyskinesia. *Cells* **8**, 1614. doi:10.3390/cells8121614

Quillin, M. L. and Matthews, B. W. (2000). Accurate calculation of the density of proteins. *Acta Crystallogr. D Biol. Crystallogr.* **56**, 791-794. doi:10.1107/S090744490000679X

Rao, V. G., Sarafdar, R. B., Chowdhury, T. S., Sivadas, P., Yang, P., Dongre, P. M. and D'Souza, J. S. (2016). Myc-binding protein orthologue interacts with AKAP240 in the central pair apparatus of the Chlamydomonas flagella. *BMC Cell Biol.* **17**, 24. doi:10.1186/s12860-016-0103-y

Roberts, A. J., Kon, T., Knight, P. J., Sutoh, K. and Burgess, S. A. (2013). Functions and mechanics of dynein motor proteins. *Nat. Rev. Mol. Cell Biol.* **14**, 713-726. doi:10.1038/nrm3667

Rupp, G., O'Toole, E. and Porter, M. E. (2001). The Chlamydomonas PF6 locus encodes a large alanine/proline-rich polypeptide that is required for assembly of a central pair projection and regulates flagellar motility. *Mol. Biol. Cell* **12**, 739-751. doi:10.1091/mbc.12.3.739

Sigrist, C. J. A., de Castro, E., Cerutti, L., Cuche, B. A., Hulo, N., Bridge, A., Bougueleret, L. and Xenarios, I. (2013). New and continuing developments at PROSITE. *Nucleic Acids Res.* **41**, D344-D347. doi:10.1093/nar/gks1067

Smith, E. F. and Lefebvre, P. A. (1996). PF16 encodes a protein with armadillo repeats and localizes to a single microtubule of the central apparatus in Chlamydomonas flagella. *J. Cell Biol.* **132**, 359-370. doi:10.1083/jcb.132.3.359

Smith, E. F. and Yang, P. (2004). The radial spokes and central apparatus: mechano-chemical transducers that regulate flagellar motility. *Cell Motil. Cytoskeleton* **57**, 8-17. doi:10.1002/cm.10155

Song, K., Awata, J., Tritschler, D., Bower, R., Witman, G. B., Porter, M. E. and Nicastro, D. (2015). In situ localization of N and C termini of subunits of the flagellar nexin-dynein regulatory complex (N-DRC) using SNAP tag and cryo-electron tomography. *J. Biol. Chem.* **290**, 5341-5353. doi:10.1074/jbc.M114.626556

Teves, M. E., Nagarkatti-Gude, D. R., Zhang, Z. and Strauss, J. F.III. (2016). Mammalian axoneme central pair complex proteins: Broader roles revealed by gene knockout phenotypes. *Cytoskeleton (Hoboken)* **73**, 3-22. doi:10.1002/cm.21271

Tinevez, J.-Y., Perry, N., Schindelin, J., Hoopes, G. M., Reynolds, G. D., Laplantine, E., Bednarek, S. Y., Shorte, S. L. and Eliceiri, K. W. (2017). TrackMate: An open and extensible platform for single-particle tracking. *Methods* **115**, 80-90. doi:10.1016/j.ymeth.2016.09.016

Trudgian, D. C. and Mirzaei, H. (2012). Cloud CPFP: a shotgun proteomics data analysis pipeline using cloud and high performance computing. *J. Proteome Res.* **11**, 6282-6290. doi:10.1021/pr300694b

Trudgian, D. C., Thomas, B., McGowan, S. J., Kessler, B. M., Salek, M. and Acuto, O. (2010). CPFP: a central proteomics facilities pipeline. *Bioinformatics* **26**, 1131-1132. doi:10.1093/bioinformatics/btq081

Trudgian, D. C., Ridlova, G., Fischer, R., Mackeen, M. M., Ternette, N., Acuto, O., Kessler, B. M. and Thomas, B. (2011). Comparative evaluation of label-free SINQ normalized spectral index quantitation in the central proteomics facilities pipeline. *Proteomics* **11**, 2790-2797. doi:10.1002/pmic.201000800

Viswanadha, R., Sale, W. S. and Porter, M. E. (2017). Ciliary motility: regulation of axonemal dynein motors. *Cold Spring Harb. Perspect. Biol.* **9**, a018325. doi:10.1101/cshperspect.a018325

Wan, K. Y., Leptos, K. C. and Goldstein, R. E. (2014). Lag, lock, sync, slip: the many 'phases' of coupled flagella. *J. R Soc. Interface* **11**, 20131160. doi:10.1098/rsif.2013.1160

Wirschell, M., Nicastro, D., Porter, M. E. and Sale, W. S. (2009). The regulation of axonemal bending. In *The Chlamydomonas Sourcebook*, 2nd edn. Vol. 3 (ed. E. H. Harris, D. B. Stern and G. B. Witman), pp. 253-282: Elsevier Inc.

Witman, G. B. (1986). Isolation of Chlamydomonas flagella and flagellar axonemes. *Methods Enzymol.* **134**, 280-290. doi:10.1016/0076-6879(86)34096-5

Witman, G. B., Plummer, J. and Sander, G. (1978). Chlamydomonas flagellar mutants lacking radial spokes and central tubules. Structure, composition, and function of specific axonemal components. *J. Cell Biol.* **76**, 729-747. doi:10.1083/jcb.76.3.729

Yokoyama, R., O'Toole, E., Ghosh, S. and Mitchell, D. R. (2004). Regulation of flagellar dynein activity by a central pair kinesin. *Proc. Natl. Acad. Sci. USA* **101**, 17398-17403. doi:10.1073/pnas.0406817101

Zhang, H. and Mitchell, D. R. (2004). Cpc1, a *Chlamydomonas* central pair protein with an adenylate kinase domain. *J. Cell Sci.* **117**, 4179-4188. doi:10.1242/jcs.01297

Zhang, Z., Zariwala, M. A., Mahadevan, M. M., Caballero-Campo, P., Shen, X., Escudier, E., Duriez, B., Bridoux, A.-M., Leigh, M., Gerton, G. L. et al. (2007). A heterozygous mutation disrupting the SPAG16 gene results in biochemical instability of central apparatus components of the human sperm axoneme. *Biol. Reprod.* **77**, 864-871. doi:10.1095/biolreprod.107.063206

Zhao, L., Hou, Y., Picariello, T., Craige, B. and Witman, G. B. (2019). Proteome of the central apparatus of a ciliary axoneme. *J. Cell Biol.* **218**, 2051-2070. doi:10.1083/jcb.201902017

Zhao, L., Hou, Y., McNeill, N. A. and Witman, G. B. (2020). The unity and diversity of the ciliary central apparatus. *Philos. Trans. R. Soc. Lond. B Biol. Sci.* **375**, 20190164. doi:10.1098/rstb.2019.0164

Zheng, S. Q., Palovcak, E., Armache, J.-P., Verba, K. A., Cheng, Y. and Agard, D. A. (2017). MotionCor2: anisotropic correction of beam-induced motion for improved cryo-electron microscopy. *Nat. Methods* **14**, 331-332. doi:10.1038/nmeth.4193

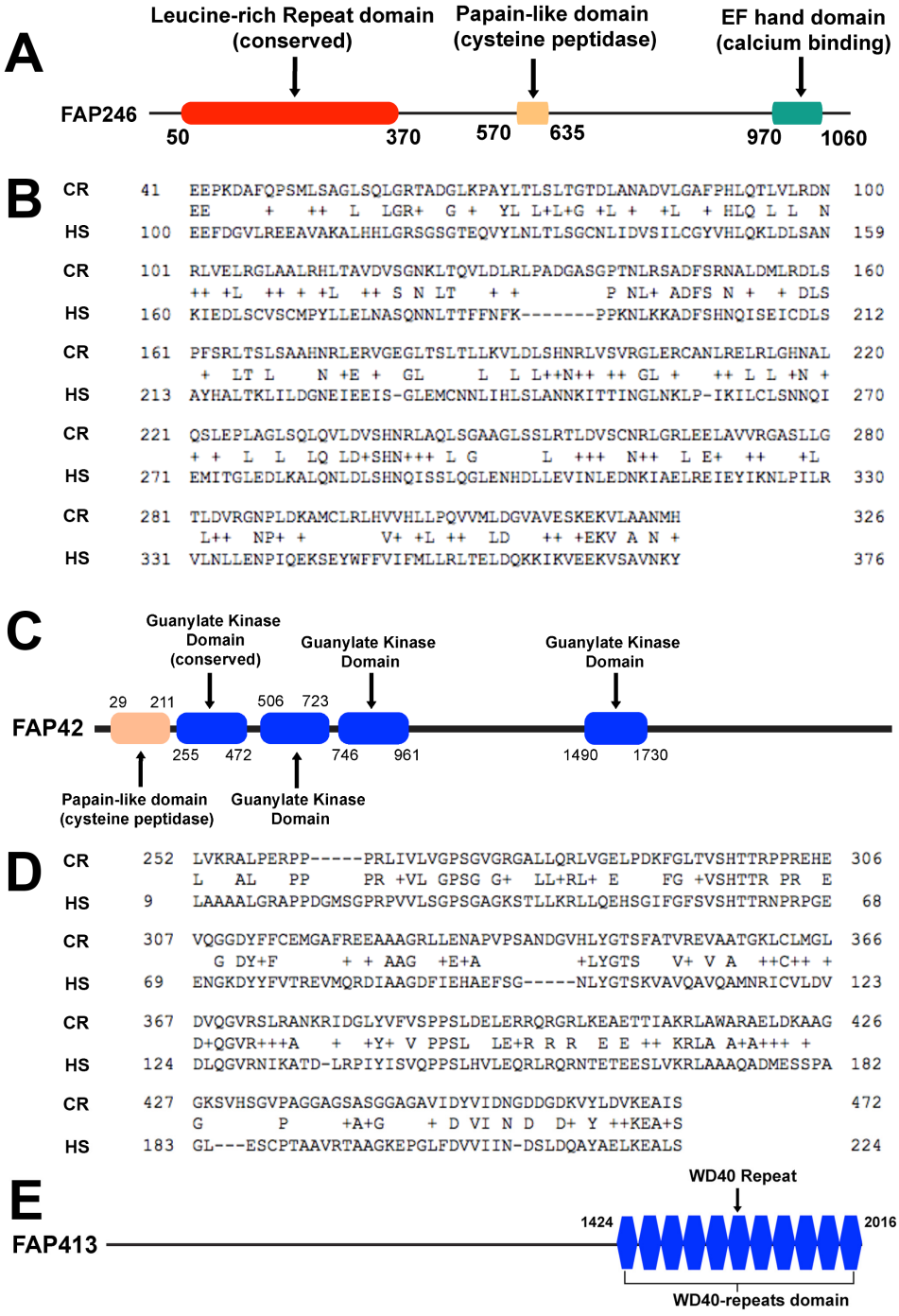

Fig. S1. Protein domain predictions and sequence alignments. **A-E)** Domain predictions for FAP246 (**A**), FAP42 (**C**) and FAP413 (**E**), and sequence alignments of FAP246 (**B**) and FAP42 (**D**) with the human proteins LRGUK-1 (NP_653249) and GUK1 (NP_000849-1) respectively. CR, *Chlamydomonas reinhardtii*; HS, *Homo sapiens*.

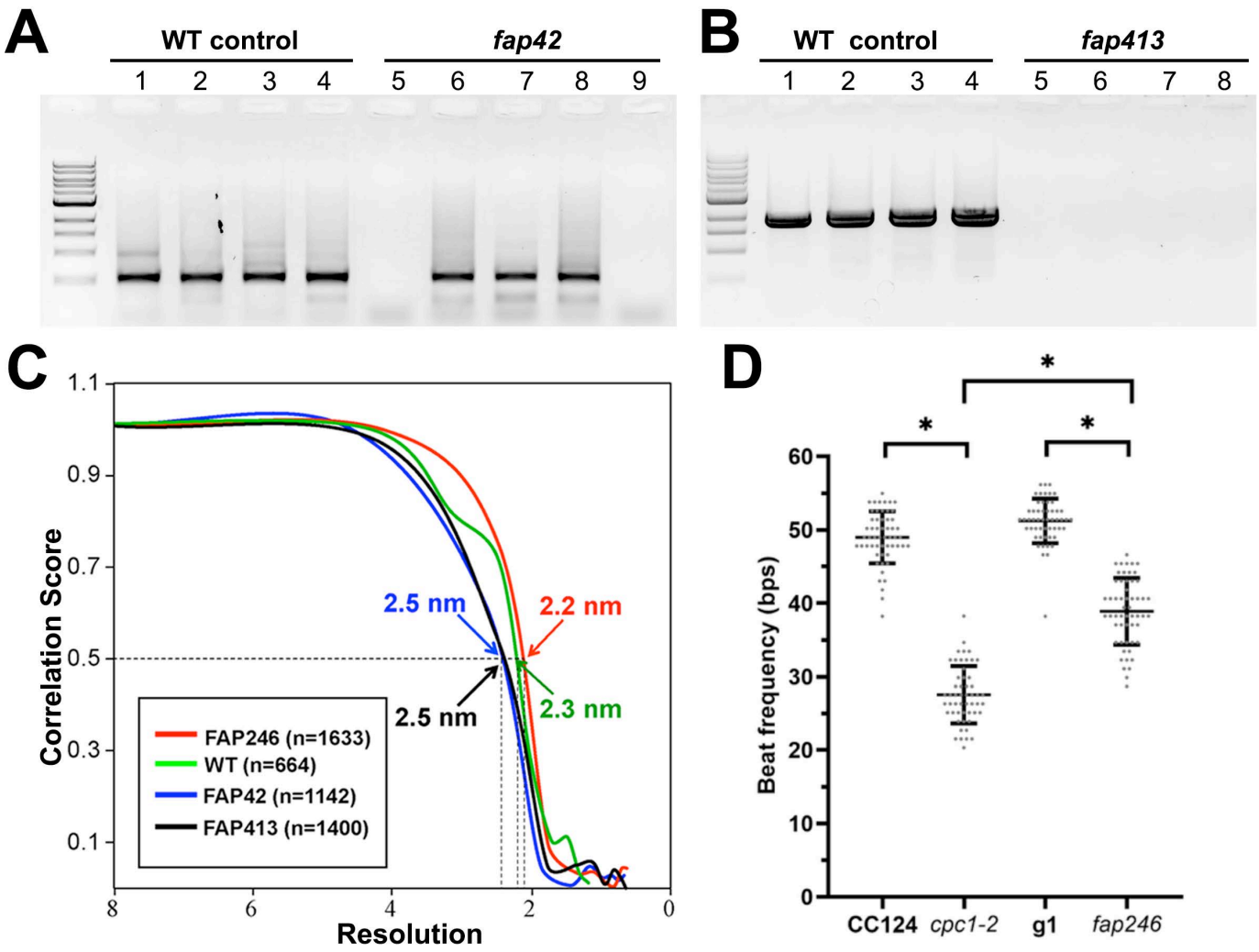

Fig. S2. Genotyping, resolution estimation and beat frequency analyses of various C1b mutants. **A-B)** Genotype analyses of the *Chlamydomonas fap42* and *fap413* CliP mutant strains. Lanes 1-4 in both **A**) and **B**) are PCR results of four WT control *Chlamydomonas* colonies, all showing an amplification product of expected size. Lanes 5-9 in (**A**) are the PCR results of five different *fap42* colonies, revealing genetic heterogeneity in the original CLiP cell line. Clones analyzed in mutant lanes 5 and 9 lack the amplification product, confirming disruption of the *FAP42* gene by the insertion cassette in these two clones. The clone of lane 5 was named "*fap42- 1*" and used for further experiments. The primer sets listed in Table S4 were used for both WT control and *fap42* PCR experiments. Lanes 5-8 in (**B**) are the PCR results of four different *fap413* colonies, all showing lack of the amplification product. The clone of lane 5 was named *fap413-1* and used for downstream

experiments. **C)** Fourier Shell Correlation (FSC) curves of the CA averages of WT (green), *fap246* (red), *fap42* (blue) and *fap413* (black) axonemes show that the resolutions are estimated to be 2.3 nm, 2.2 nm, 2.5 nm and 2.5 nm (0.5 criterion), respectively. **D)** Scatterplots showing flagellar beat frequencies of *cpc1* and *fap246* mutants and their respective parental strains CC-124 and g1. For each strain, the solid bars show mean and standard deviation. Significant differences (Student's t test, $P<0.01$) between strains are indicated by *.

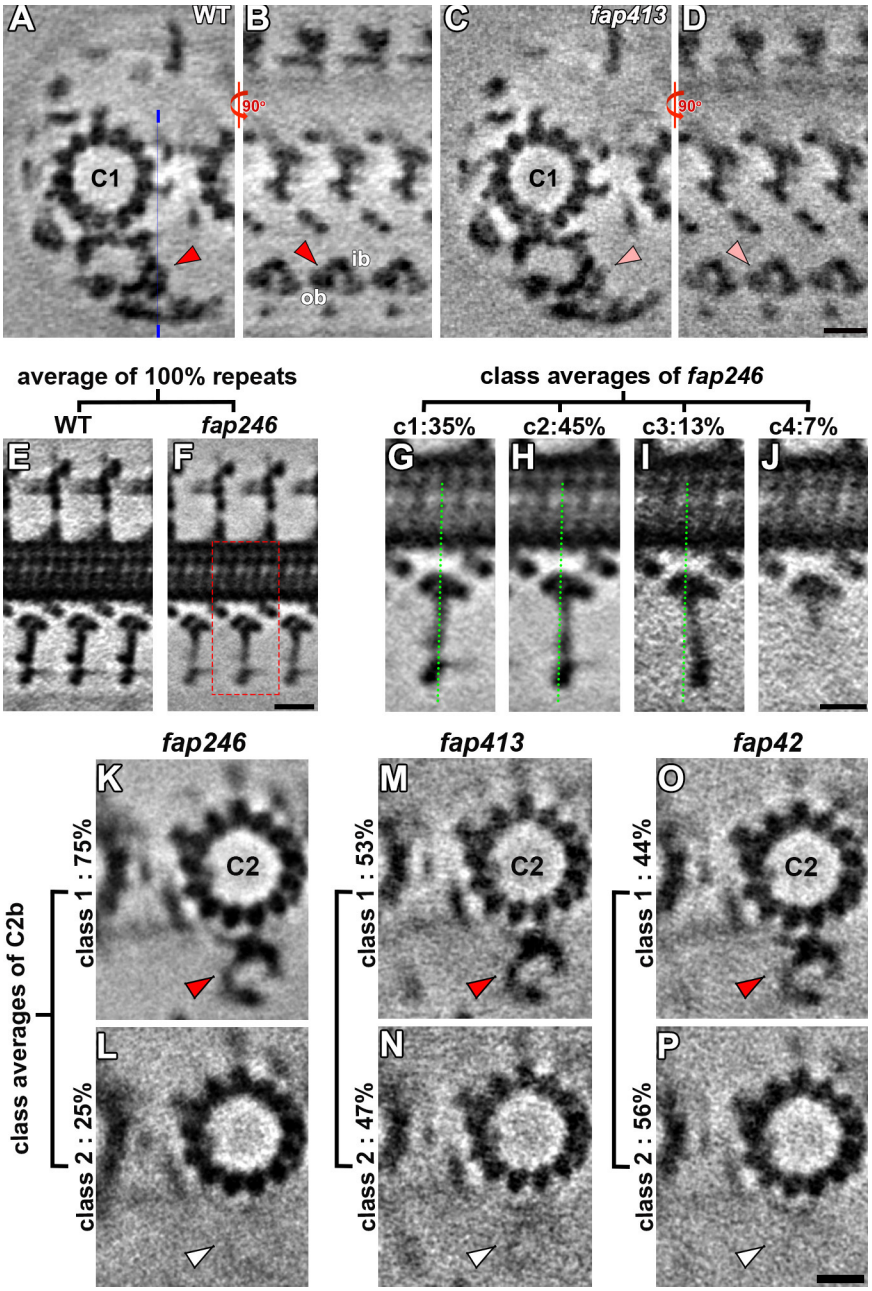

Fig. S3. Cryo-ET and subtomogram averaging localized FAP413 to the C1b projection, classification analyses of the pillar density of the *fap246* CA revealed positional flexibility, and classification analyses of the CA of all three C1b mutants revealed partial loss of the C2b density. A-D) Tomographic slices of the averaged CA repeats of WT (**A** and **B**) and *fap413* (**C** and **D**) in cross-sectional (**A** and **C**) and longitudinal views (**B** and **D**) show that the outer bracket (ob) density is fully present in the wild-type CA (red arrowheads) but significantly weakened in *fap413* (pink arrowheads). The thin blue line in (**A**) indicates the locations for the

slices shown in (**B** and **D**). Other labels: ib, inner bracket. Scale bar: 10 nm (in **D** valid for **A**-**D**). **E**-**J**) Classification analyses revealed structural heterogeneity in the *fap246* but not the WT C1b projection. Longitudinal tomographic slices of the averages that included all CA repeats showed that the pillar density was blurred in the *fap246* mutant (**F**) compared to WT (**E**). Classification analyses focused on the pillar density revealed four distinct classes (percentages of repeats are indicated for each class) (**G**-**J**). The regions shown in (**G**-**J**) are indicated by the red dotted box in (**F**). The green dotted lines serve as references to show the positional differences between classes. Scale bars: 10 nm (in **F** valid for **E** and **F**); 5 nm (in **J** valid for **G**-**J**). **K**-**P**) Classification analyses focused on the C2b density of the CA averages of *fap246* (**K**-**L**), *fap413* (**M**-**N**) and *fap42* (**O**-**P**) all revealed two distinct classes (percentages of repeats are indicated for each class). In the cross-sectional views for each mutant, the density is present (red arrowheads) in class 1 and missing (white arrowheads) in class 2. Scale bars: 10 nm (in **P** valid for **K**-**P**).

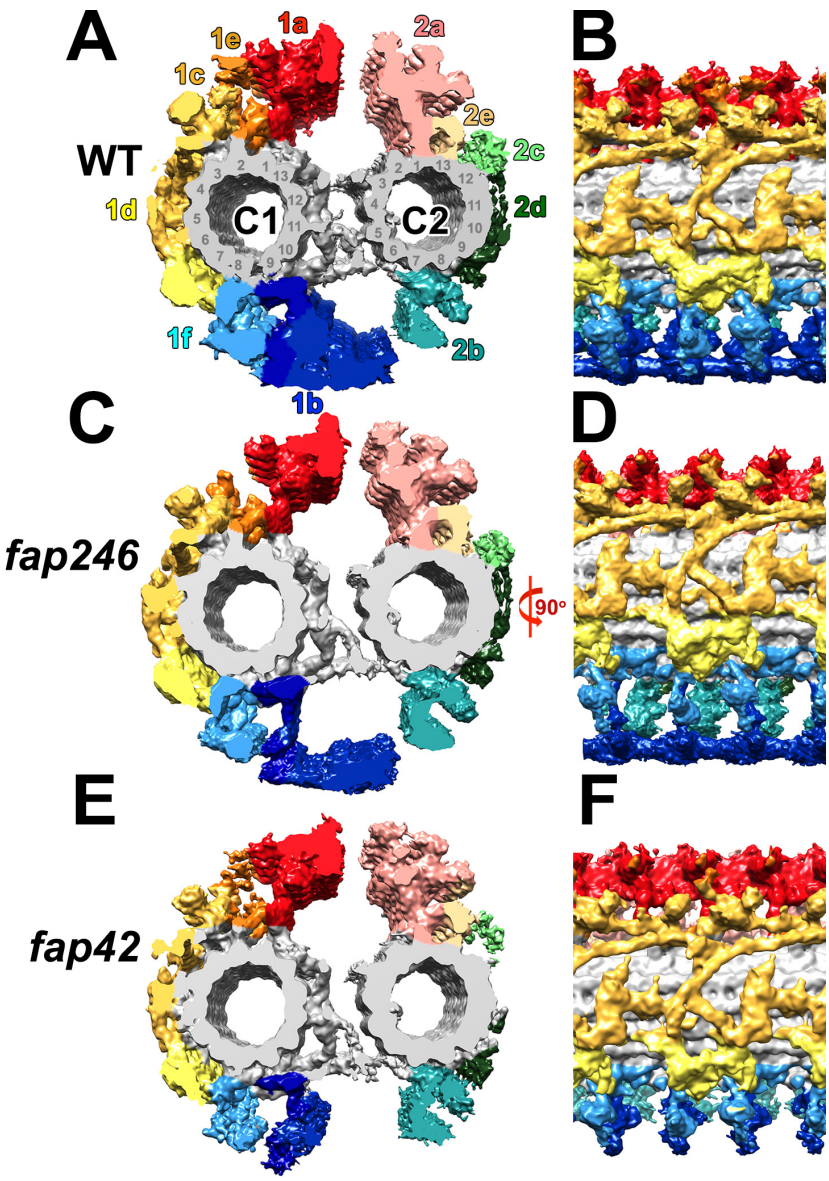

Fig. S4. Averaged CA repeats of WT, *fap246* and fap42 revealed structural defects of the indicated mutants. A-F) Isosurface renderings showing the *entire* averaged CA repeats (as compared to partial views in various main figures) of WT (**A** and **B**), *fap246* (**C** and **D**), and *fap42* (**E-F**) viewed in cross-sectional (**A**, **C** and **E**) and longitudinal orientations (**B**, **D** and **F**).

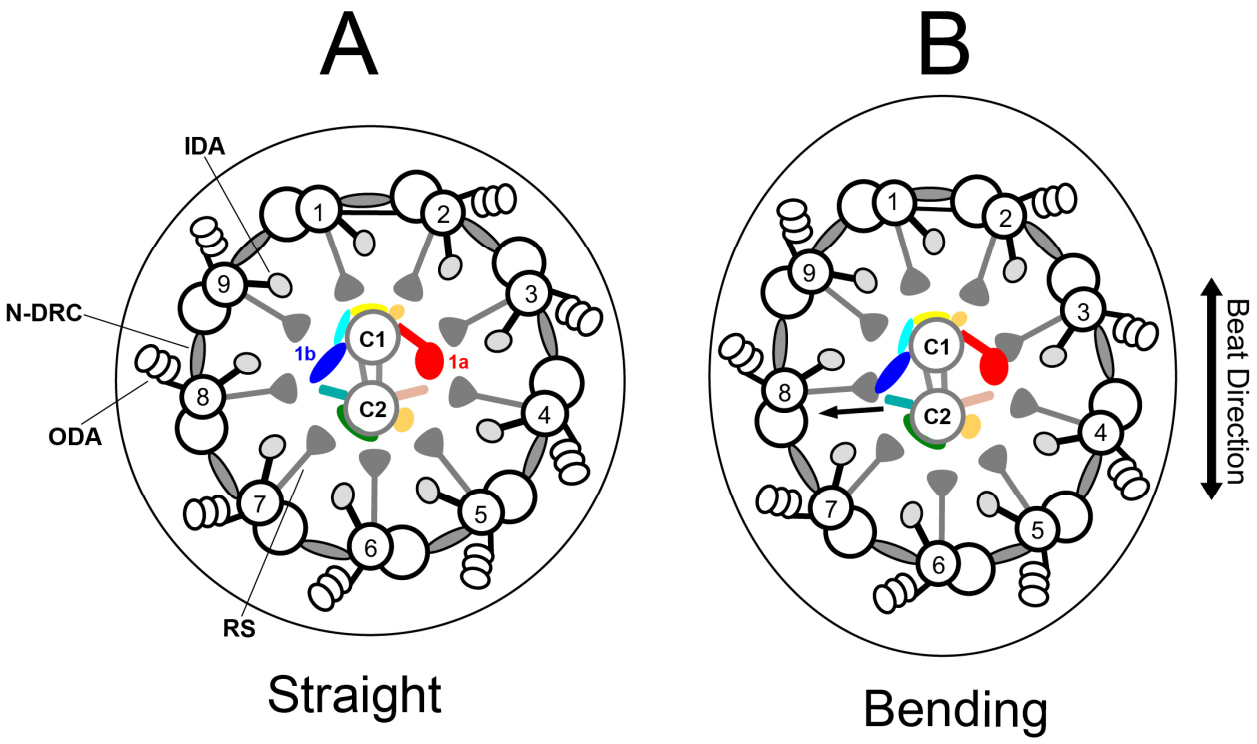

Fig. S5. Model depicting how the C1b projection may resist compression force during axonemal bending and how CA-RS mechano-signaling may transmit signals to regulate dynein activity and ciliary motility. A) In a straight flagellum, the 9 DMTs of the axoneme are cylindrically arranged around the CA, and all RS heads are equally distant from the circumference of the CA, i.e. the outermost periphery of the CA projections. **B)** In bent regions of a *Chlamydomonas* flagellum, the C1 and C2 microtubules are both in the plane of bend and, at least in the principal bend, C1 is on the outside of the bend, facing DMT 1 (Mitchell, 2003). When the flagellum bends, the axoneme becomes wider in the plane of bend (Lindemann and Mitchell, 2007), causing the RS heads to mechanically push against the C1a (red) and C2a (pink) projections on one side of the CA and the C1b (dark blue) and C2b (light green) projections on the opposite side. The pillar-bracket-beam structure of the C1b projection provides structural stability that likely resists this mechanical force (arrow). This mechanical interaction between the CA and RSs also could play a role in transmitting signals that regulate dynein activity and thus ciliary beating. In both panels, the axoneme is viewed from inside the cell. DMTs are numbered according to (Hoops and Witman, 1983); the black line between DMTs 1 and 2 represents the peripheral link between these two DMTs.

Table S1. MS/MS analyses of the axonemes of the *fap246*, *fap413* and *fap42* mutants — CA proteins assigned to C1a, C1c, C1d, C1e and C2b, or that were not previously confirmed to be components of a specific CA projection.

Protein	CA projection	Phytozome gene number	MW (kDa)	No. of Unique Peptides				Quantification Ratio		
				WT	*fap*246	*fap413*	*fap42*	*fap*246/WT	*fap42*/WT	*fap*413/WT
CA proteins[a]										
FAP54	C1d	Cre12.g518550	319	121	127	121	125	1.05	1.13	0.99
FAP46	C1d	Cre10.g420800	291	123	124	123	126	1.00	1.10	1.00
FAP221	C1d	Cre11.g476376	71	25	24	22	24	0.95	1.04	0.67
FAP297	C1d	Cre01.g029350	74	41	41	41	43	0.92	0.96	0.94
FAP74	C1d	Cre06.g271150	200	64	66	66	67	1.07	1.17	1.05
PF6	C1a	Cre10.g434400	237	100	104	107	107	1.11	1.05	1.05
PF16	C1a	Cre09.g394251	50	26	25	29	24	0.97	0.91	1.08
FAP92	C1a	Cre13.g562250	150	60	59	60	66	1.16	1.06	0.99
FAP101	C1a	Cre02.g112100	86	27	27	26	27	1.01	1.04	0.81
FAP119	C1a	Cre06.g256450	34	12	12	13	12	1.13	0.81	0.85
FAP227	C1a	Cre17.g729850	17	17	17	17	16	1.01	0.96	0.91
FAP114	C1a	Cre09.g389282	32	15	14	17	13	0.91	0.79	0.59
FAP81	C1e	Cre06.g296850	172	68	68	73	68	1.07	1.06	1.36
FAP216	C1c	Cre12.g497200	79	33	31	32	31	0.74	0.89	0.87
FAP76	C1c	Cre09.g387689	162	76	82	79	76	1.11	1.02	0.87
Hydin	C2b	Cre01.g025400	528	209	217	227	212	1.06	1.16	1.14
FAP7[a]	?	Cre12.g531800	55	23	24	27	26	1.01	1.24	1.33
FAP47[a]	?	Cre17.g704300	310	120	126	136	123	1.07	1.09	1.34
FAP49[b]	C2	Cre08.g362050	295	35	32	36	40	0.98	1.29	1.22
FAP65[a]	C2	Cre07.g354551	220	69	75	82	69	1.15	1.05	1.54
FAP70[a]	C2	Cre07.g345400	114	41	43	46	42	1.17	1.10	1.36
FAP72[b]	?	Cre08.g362000	595	32	35	33	40	1.36	1.28	1.03
FAP75[a]	C2	Cre06.g249900	125	40	40	38	38	0.91	0.88	1.22
FAP99[a]	C1	Cre14.g624400	90	50	53	58	53	1.22	1.21	0.94
FAP105[a]	C1	Cre12.g511750	31	23	20	24	18	0.74	0.67	0.78
FAP108[a]	C1	Cre06.g297200	22	11	13	12	11	0.93	0.94	0.68
FAP123[a]	?	Cre03.g171800	34	18	19	20	19	0.94	0.79	1.32
FAP125[a]	?	Cre12.g546100	112	62	63	64	68	1.13	1.29	0.82
FAP139[b]	?	Cre09.g387912	76	30	31	34	32	1.04	1.13	1.05
FAP147[a]	C2	Cre04.g224250	97	41	48	40	42	1.43	1.16	1.83
FAP154[b]	?	Cre08.g362100	467	42	52	41	58	1.25	1.36	0.63
FAP171[a]	C2	Cre14.g624900	81	23	22	26	26	0.83	0.87	0.51

FAP174[b]	?	Cre02.g105950	10	6	6	7	5	1.09	0.71	0.81
FAP178[b]	C2	Cre10.g418150	20	6	6	7	5	0.87	0.51	0.60
FAP194[a]	?	Cre12.g522150	52	26	26	27	28	0.95	0.98	1.03
FAP225[a]	?	Cre01.g051050	81	42	45	48	41	1.14	0.88	1.18
FAP239[a]	C2	Cre03.g145387	23	13	15	16	14	1.20	1.12	1.29
FAP266[a]	?	Cre16.g690450	22	5	7	8	5	1.02	0.99	0.94
FAP275[b]	C1	Cre05.g239200	18	10	8	10	8	0.72	0.68	0.97
FAP286[b]	C2	Cre12.g509800	17	11	13	19	9	1.11	0.64	1.26
FAP289[a]	C1	Cre01.g009800	46	19	18	22	20	1.06	1.17	1.09
FAP312[a]	C2	Cre14.g630200	34	41	40	40	39	0.92	0.83	1.06
FAP345[b]	C1	Cre15.g640000	13	29	33	36	31	1.39	1.19	1.30
FAP348[b]	C1	Cre16.g693204	96	35	32	36	35	0.70	1.05	1.58
FAP380[b]	?	Cre01.g010400	20	7	7	7	4	0.53	0.40	0.73
FAP411[b]	C1	Cre09.g409600	13	13	11	12	14	0.82	1.21	1.08
FAP412[a]	C1	Cre12.g497450	57	24	22	24	20	0.85	0.63	0.96
FAP416[b]	?	Cre17.g697750	17	2	2	2	2	1.22	1.27	1.25
DIP13[b]	?	Cre17.g724550	13	10	8	13	8	0.81	0.77	1.58
DPY30[b]	C1	Cre06.g279100	11	5	5	5	4	0.83	0.66	0.73
MOT17[a]	C1	Cre11.g482300	47	23	23	27	21	0.25	0.27	0.58
FAP173[c]	?	Cre16.g690879	33	15	10	11	14	0.25	0.27	0.58
FAP209[c]	C1c	Cre02.g147750	111	43	44	43	47	1.77	1.23	3.87
FAP219[c]	C1c	Cre16.g650450	25	18	17	17	18	0.81	0.88	1.03
FAP244[c]	C2	Cre08.g374700	178	55	56	58	55	1.06	1.01	1.29
FAP279[c]	C1d	Cre06.g268650	30	14	16	18	16	1.12	1.14	0.98
FAP331[c]	C1b/f	Cre06.g308000	205	89	89	88	91	1.04	0.96	1.48
FAP401[c]	C1a/e	Cre12.g529700	101	39	38	38	40	0.88	0.89	1.75

[a]Novel proteins that are predicted to be CA proteins by both (Zhao et al., 2019) and (Dai et al., 2020).

[b]Novel proteins that are predicted to be CA proteins only by (Zhao et al., 2019).

[c]Novel proteins that are predicted to be CA proteins only by (Dai et al., 2020).

Table S2. Exclusive unique FAP246 and FAP413 peptides identified in the proteomic analyses of *fap246* axonemes

Protein	Peptide Sequence	Start residue number	End residue number
FAP246	TADGLKPAYLTLSLTGTDLANADVLGAFPHLQTLVLR	62	98
	SLPPPPPPEPVEEPK	30	44
	PSDGASVAGSSR	2	13
	NALDMLR	151	157
	LTSLSAAHNR	165	174
	LPADGASGPTNLR	132	144
	HLTAVDVSGNK	113	123
	DAFQPSMLSAGLSQLGR	45	61
FAP413	AGLLDLLR	1126	1133
	SLVSGSEDKTLR	1442	1453

Table S3. Exclusive unique FAP42 and FAP413 peptides identified in the proteomic analyses of *fap42* axonemes

Protein	Peptide Sequence	Start residue number	End residue number
FAP42	AALQAAWAAGK	1690	1770
	AQVAGQLVLEAFDWR	1927	1949
	DALYVFVASPGQLR	906	919
	DGSTLVLDPTAQLR	2401	2414
	DLEGSLQAGHR	123	130
	EAEAAAAEAAMK	925	936
	EAISTLSPIIR	510	520
	EFPDVFAYPR	570	579
	EMEAAAAAGSPFDATIVNDDPEAAYAELTR	732	761
	GAGTTAITNAALLR	863	872
	GVNEEGTYCLTVTCTSPLAGAAAGAGALTEVPCHR	2101	2135
	HAVAAVTLVK	286	295
	LALSDAHVAALR	1418	1429
	LHATELPASGAGYCLLALYDTGSR	2077	2100
	LIVLVGPSGVGR	306	317
	LPVVEGPLELALALK	1701	1715
	LRDHLTETDEEIAAR	711	725
	MLLQQLGEQLELVPVVTSRPPLR	1595	1617
	NVLVLAGPAGVGK	1577	1589
	QQLLQLQQDDGR	1489	1500
	REMEAAAAAGSPFDATIVNDDPEAAYAELTR	731	761
	RIDGLYVFVSPPSLDELER	420	438
	RPEELVLNSPDVPMVTTVAPPPPPEPTGGK	72	101
	SCTVLADNALAK	2297	2300
	TLMANAGLLELPR	1958	1968
	VALLYVDSPEPVK	1460	1472
	VLPAGGKPGSGPVLLSAEQLAER	2332	2354

	VPELAVVPSTSLK	1379	1391
	YGEAPAGAVGVLFR	1935	1948
FAP413	VQPAAAAAYEAQDDLR	423	438
	VLDSVASSSEALQELQPR	94	111
	SVVSGSLDSTLR	1791	1802
	SLVEGVGDTLAR	328	339
	LPLSQAFEWLLEAPLNR	923	939
	INVVSSVCFSPDGR	1643	1456
	FGAGSWLR	373	380
	DLEGPLAGLTAHLR	351	364
	ASAEATKPNQQQR	14	26
	APTGTAVFQEAR	1377	1388

Table S4. Primers used in this study to confirm the mutant insertion site

Name	Sequence (5'-3')	Sequence (3'-5')
fap246	TGTTGTGCCGCGCCTGCGAG	TCTTGGCTCAGCGGCTCTTG
fap413	ACATTGCCCTCAACAAGACC	TGATAGGACTCGGGATGGAG
fap42	GCCTACCTGTTCATTGGCAT	GCCTACCTGTTCATTGGCAT

Table S5. Summary of image processing information for the strains used in this study

Strains	**Number of Tomograms**	**Number of averaged CA repeats**	**Resolution (nm)**	**TEM/Camera**
WT	14	664	2.3	Krios/K2/VPP
fap246	38	1633	2.2	Krios/K3/VPP
fap413	30	1401	2.5	Krios/K3/VPP
fap42	25	1142	2.5	Krios/K3/VPP

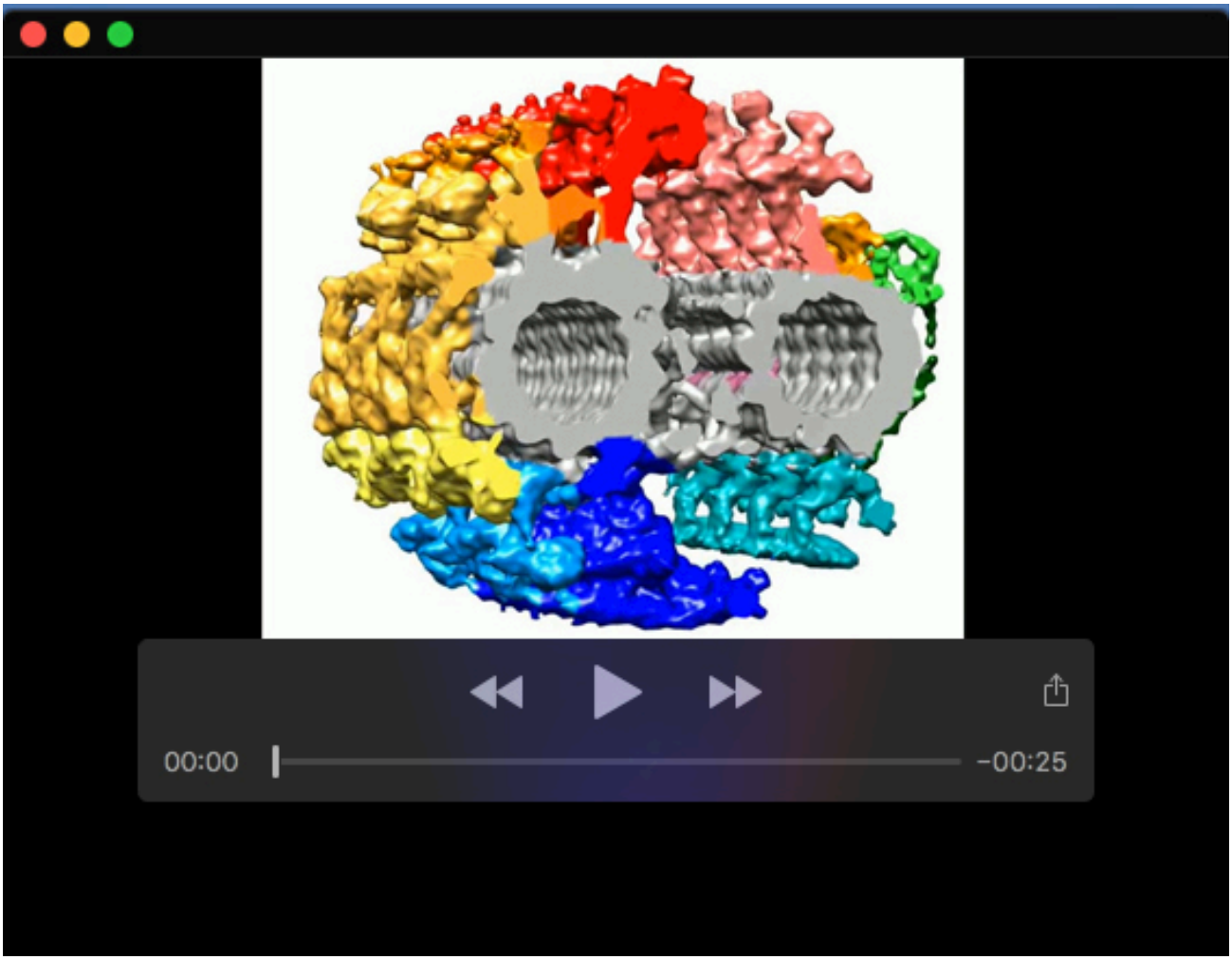

Movie 1. Animated 3D visualization of the averaged repeats of the *Chlamydomonas* WT CA. The averaged CA repeats are shown in cross-sectional orientation at the beginning of the animation. The CA projections associated with the C1 and C2 microtubules are indicated (nomenclature and color coding follow that of (Carbajal-Gonzalez et al., 2013) and (Fu et al., 2019)).

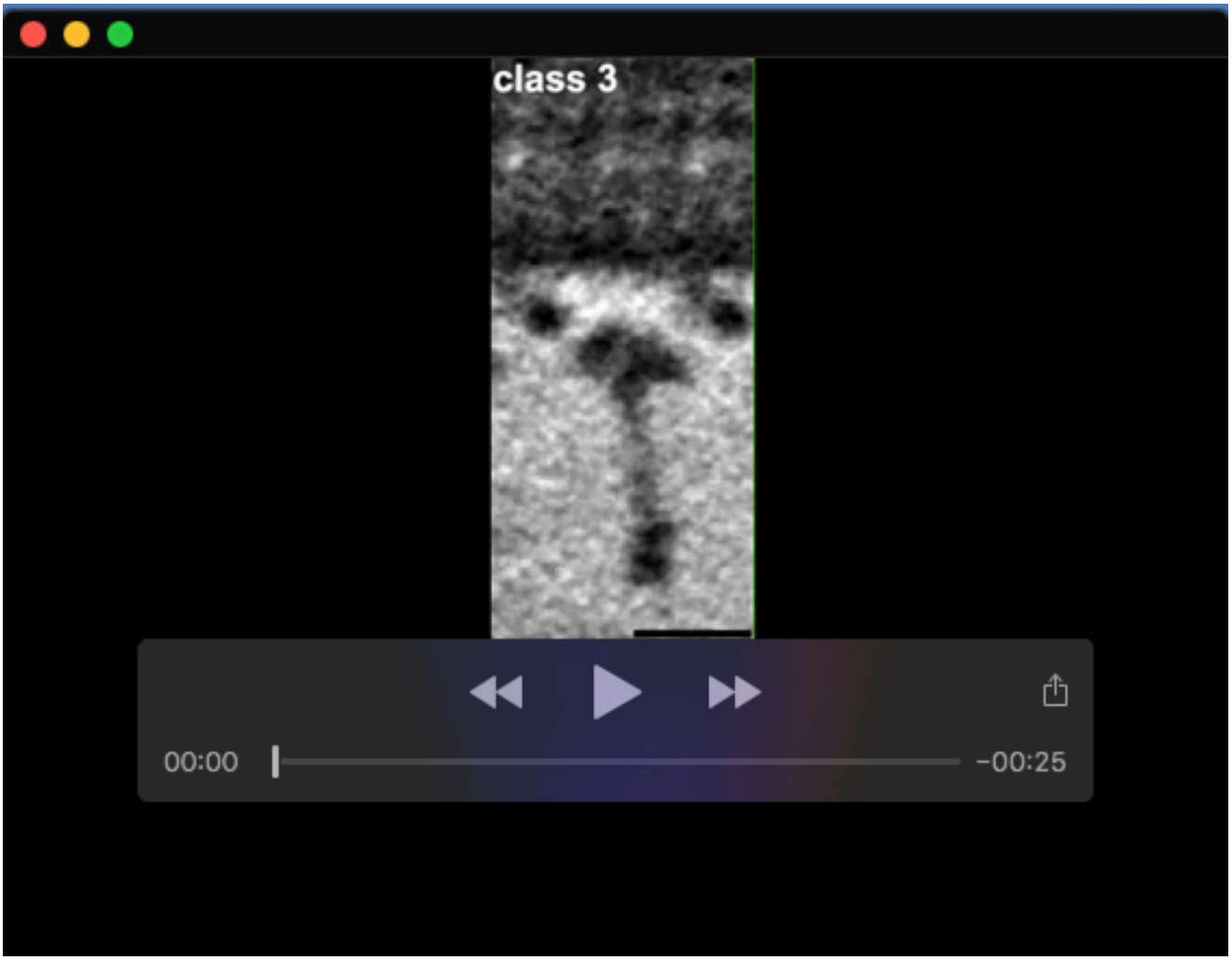

Movie 2. Comparison of the four class averages of the *fap246* CA shows positional flexibility of the C1b projection. Sequence of one tomographic slice for each class average in longitudinal orientation. Related to Fig. 2. Scale bar: 10 nm.

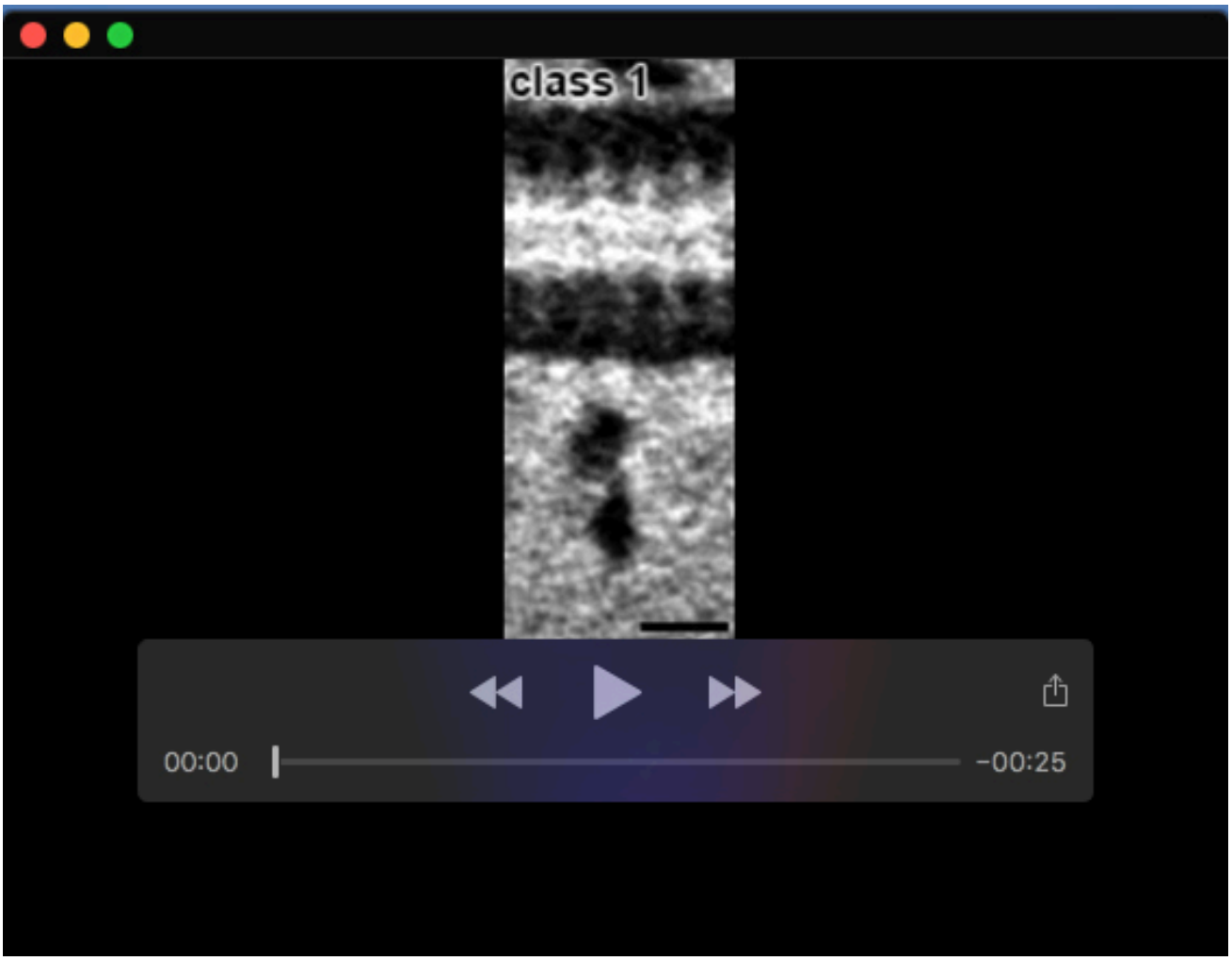

Movie 3. Comparison of the three class averages of the *fap42* CA shows positional flexibility of the C1f projection. Sequence of one tomographic slice for each class average in longitudinal orientation. Related to Fig. 4. Scale bar: 10 nm.

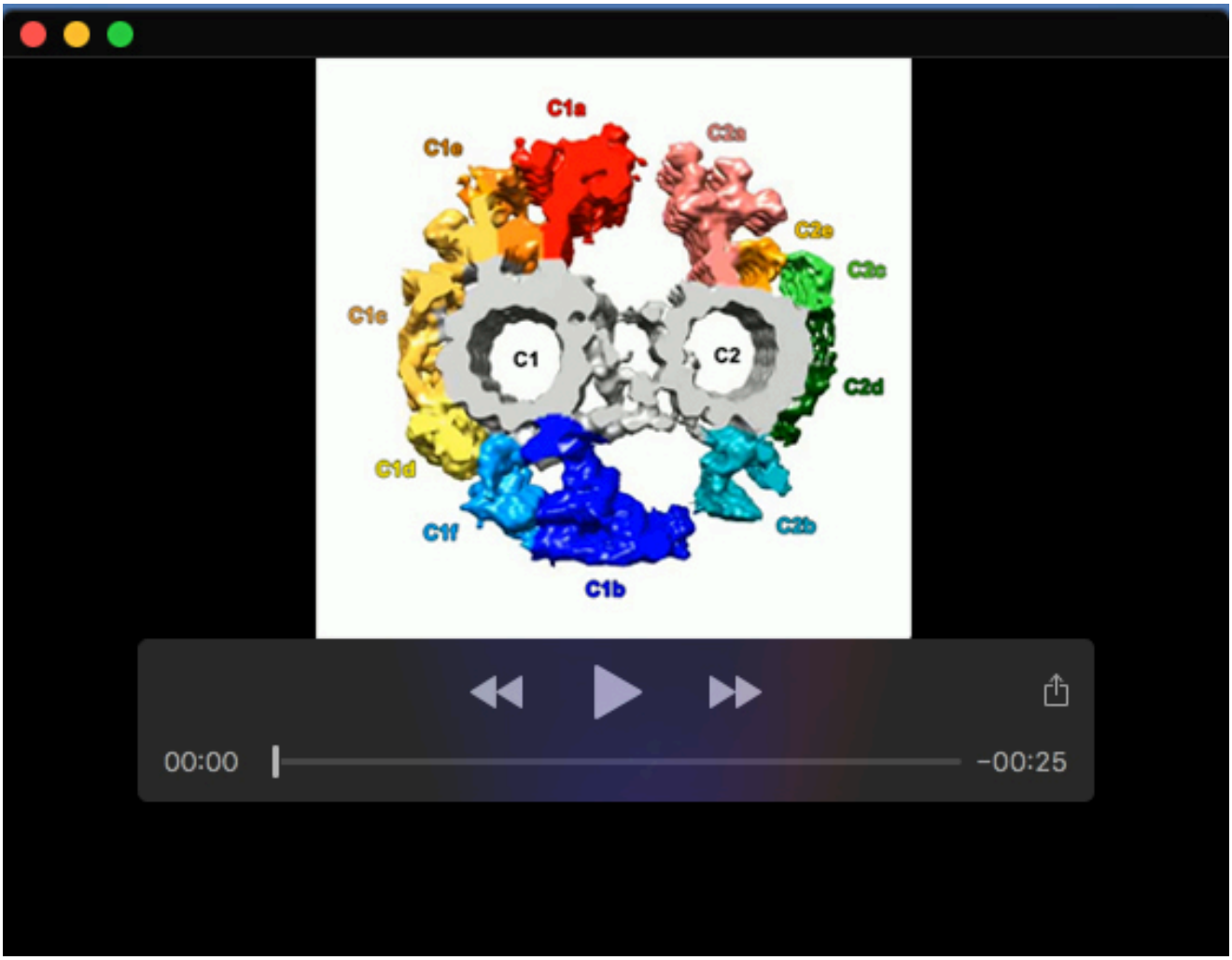

Movie 4. Animated 3D visualization of the averaged repeats of the *Chlamydomonas* WT CA highlighting the locations of FAP246, FAP413, and FAP42 within the C1b projection. Nomenclature and color coding of the CA projections are indicated.

Supplementary References:

Carbajal-Gonzalez, B. I., Heuser, T., Fu, X., Lin, J., Smith, B. W., Mitchell, D. R. and Nicastro, D. (2013). Conserved structural motifs in the central pair complex of eukaryotic flagella. *Cytoskeleton (Hoboken)* **70**, 101-120.

Dai, D., Ichikawa, M., Peri, K., Rebinsky, R. and Bui, K. (2020). Identification and mapping of central pair proteins by proteomic analysis. *Biophysics and Physicobiology* **17** 71-85.

Fu, G., Zhao, L., Dymek, E., Hou, Y., Song, K., Phan, N., Shang, Z., Smith, E. F., Witman, G. B. and Nicastro, D. (2019). Structural organization of the C1a-e-c supercomplex within the ciliary central apparatus. *J Cell Biol* **218**, 4236-4251.

Hoops, H. J. and Witman, G. B. (1983). Outer doublet heterogeneity reveals structural polarity related to beat direction in Chlamydomonas flagella. *J Cell Biol* **97**, 902-8.

Lindemann, C. B. and Mitchell, D. R. (2007). Evidence for axonemal distortion during the flagellar beat of Chlamydomonas. *Cell Motil Cytoskeleton* **64**, 580-9.

Mitchell, D. R. (2003). Orientation of the central pair complex during flagellar bend formation in Chlamydomonas. *Cell Motil Cytoskeleton* **56**, 120-9.

Zhao, L., Hou, Y., Picariello, T., Craige, B. and Witman, G. B. (2019). Proteome of the central apparatus of a ciliary axoneme. *J Cell Biol* **218**, 2051-2070.